Phys. Status Solidi A **214,** No. 1, 1600410 (2017) / **DOI** 10.1002/pssa.201600410

physica status solidi a
www.pss-a.com
applications and materials science

Review Article

Selective emitters for thermophotovoltaic applications

Nicole A. Pfiester and Thomas E. Vandervelde*

Department of Electrical Engineering, Tufts University, 161 College Ave., Medford, Massachusetts 02155, USA

Received 29 May 2016, revised 28 September 2016, accepted 29 September 2016
Published online 7 November 2016

Keywords metamaterials, optical absorbers, photonic crystals, rare earths, thermophotovoltaics

* Corresponding author: e-mail tvanderv@ece.tufts.edu, Phone: +00 617 627 3217, Fax: +00 617 627 3220

Applying thermophotovoltaic (TPV) technologies to existing energy generators allows us to increase energy output while utilizing present infrastructure by reclaiming the heat lost during the production process. In order to maximize the efficiency of these sources, the conversion efficiency of the TPV system needs to be optimized. Selective emitters are often used to tailor the spectrum of incident light on the diode, blocking any undesirable light that may lead to device heating or recombination. Over the years, many different technologies have been researched to create an ideal selective emitter. Plasmas and rare-earth emitters provided highly selective spectra early on, but their fixed peaks required tailoring the diode's band gap to the emitter's characteristic wavelength. Recent advances in engineerable materials, such as photonic crystals and metamaterials, allow the opposite to take place; an appropriate selective emitter can be designed to match the TPV diode, allowing the diode structure to be optimized independently from the emitter.

1 Introduction Thermophotovoltaics (TPV), an infrared radiation to electricity conversion technology, can not only make use of parts of the solar spectrum untouched by traditional PV systems, they also allow conversion of other forms of heat from combustion sources or pre-existing warm bodies. One such application is to collect waste heat from high temperature fabrication or electricity production processes and convert it into electricity [1–3]. Use of a specialized emitter stage as part of a complete TPV system enables the use of waste heat to generate the photons necessary to complete the photovoltaic process. A TPV system, consisting of an emitter stage, a filter, and a TPV diode, is energy agnostic, so it generates electricity in the same way regardless if the power source is the Sun, a smelting furnace, a decaying radioactive particle, or a combustion source. Compared to direct-conversion photovoltaic devices, like traditional solar PV, TPV systems that utilize the Sun, or solar TPV systems, are capable of capturing greater amounts of energy, according to the theoretical efficiency maximum of up to 60% under full sun concentration [4]. More broadly, TPV systems can be tailored to any temperature range, providing more opportunities to generate electricity.

As TPV technology is very similar to PV, it is of no surprise that the first evidence of thermal to electric conversion came from experiments with a silicon PV cell and small combustion source. In 1956, Henry Kolm of MIT's Lincoln Lab measured the power from a silicon cell held to a gas lantern [5]. However, significant growth in TPV research did not begin until Pierre Aigrain presented a series of lectures on the topic at MIT in the early 1960s [1]. Interest from the US Army and General Motors through the 1960s and early 1970s added developments, such as rare earth thermal emitters [6] and back surface reflector spectral control [7], to the TPV arsenal. This research slowed significantly through the mid-1970s as the Army turned more to thermoelectric power generation [8]. Fabrication improvements for III–V materials led to a renewed interest in TPV in the 1990s that continues through today [8]. The narrow band gaps that can be created using III–V combinations are better suited for the infrared range than the previously used silicon or germanium cells. The small band gaps utilized in these devices are prone to detrimental recombination effects and parasitic heating; however, spectral control methods such as filters and selective emitters are used to combat these problems. How these are applied in reference to the full TPV system can be seen in Fig. 1.

As a whole, TPV systems have reached efficiencies greater than 20% [10]. Individual TPV cell conversion

efficiencies are often much higher than this for a narrow band, but the overall system efficiency is brought down by the emitter, cavity, or filter not being 100% efficient. Due to the wide variety of TPV applications and the configurations and design of TPV systems, direct comparison of efficiency calculations can be difficult. Any reported efficiency value should be regarded in context with the heat source, type and design of emitter, filter performance, and diode design.

1.1 TPV system Though it is possible to operate the TPV diode on its own like with traditional PV, real world performance improves when it is used as part of a TPV system. Such a system consists of the TPV diode with an emitter and a filter for spectral control. Each stage has its own design considerations and can be tailored to the application at hand. Example configurations for three of the primary uses of TPV are shown in Fig. 2. Notice that once the power from the source is absorbed by the emitter, the TPV system setup is the same.

1.1.1 Diode Common solar PV materials such as silicon and germanium can be used for TPV diodes, but higher efficiencies can be achieved with III–V materials. The lower band gaps of these materials, like the 0.72 eV (1.7 μm) gap of GaSb, better utilize longer wavelengths. The renewed TPV interest of the 1990s was spurred by improved III–V growth techniques, leading to TPV diodes made of GaSb [12–15] as well as more complex ternary and quaternary compounds [16–18]. Though the creation of tandem and multijunction cells is a common efficiency boosting technique in solar PV, similar outcomes can be achieved in TPV with spectral control rather than difficult epitaxial growths. Even so, GaInP/GaAs [19], AlGaAsSb/GaSb [20], GaInAsSb/InAsSb [21], and other heterojunction [22] TPV cells have been reported. Theoretical studies have shown multijonction TPV diodes could achieve higher efficiencies than single junction cells [23] and help mitigate the power versus efficiency tradeoff that often occurs in TPV systems [24].

Monolithically interconnected modules (MIMs), subcells fabricated next to each other on the same material, can also be used to increase TPV diode output. The subcells are wired in series to make a larger TPV cell with a higher operating voltage, an important improvement since TPV voltages are typically low due to the narrow band gaps [25]. Higher output power densities, improved thermal coupling, and higher system efficiency are also achieved due to decreased joule heating from lower currents and improved

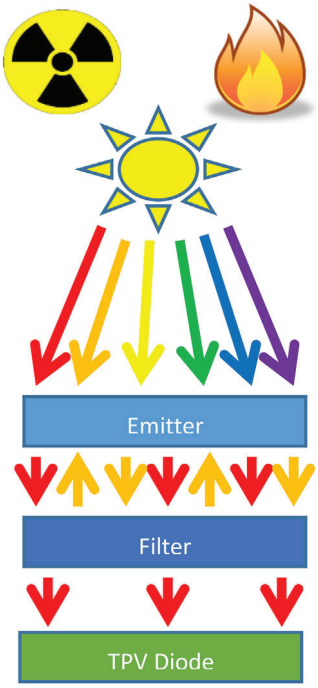

Figure 1 Several forms of spectral control are used to make the most efficient use of the energy source and the TPV diode. The emitter stage absorbs heat from radiation, convection, and conduction and then radiates, in the case of a selective emitter, a narrowband spectrum toward the TPV diode. The filter further refines the spectrum so only photons near the band gap hit the diode. Reproduced with permission [9]. Copyright 2015, EUPVSEC.

Nicole A. Pfiester is a National Science Foundation Graduate Research Fellow and Future Leader of Engineering Fellow while pursuing her Ph.D. at Tufts University, USA. She received her B.S. in Physics from Purdue University and her M.S. in Electrical Engineering from Tufts University. Nicole's research interests include the design and fabrication of metamaterial technologies for optoelectronic applications such as photodetectors and thermophotovoltaics, as well as the development and fabrication of photonic devices.

Thomas E. Vandervelde is an Associate Professor in the Electrical and Computer Engineering Department at Tufts University, USA. He received his Ph.D. in Physics from the University of Virginia in 2004 and completed post-doctoral research at UVa, the University of Illinois Urbana-Champaign, and a joint position between Sandia National Labs and University of New Mexico. He received awards that include the NSF CAREER Award, AFOSR Young Investigator Research Program Award, Intelligence Community Young Investigator Award, and Alexander von Humboldt Award for Experienced Researchers. Tom's research focuses on optoelectronic materials and devices, with a particular emphasis on structured materials (e.g. metamaterials), photovoltaics, thermophotovoltaics, and photodetectors.

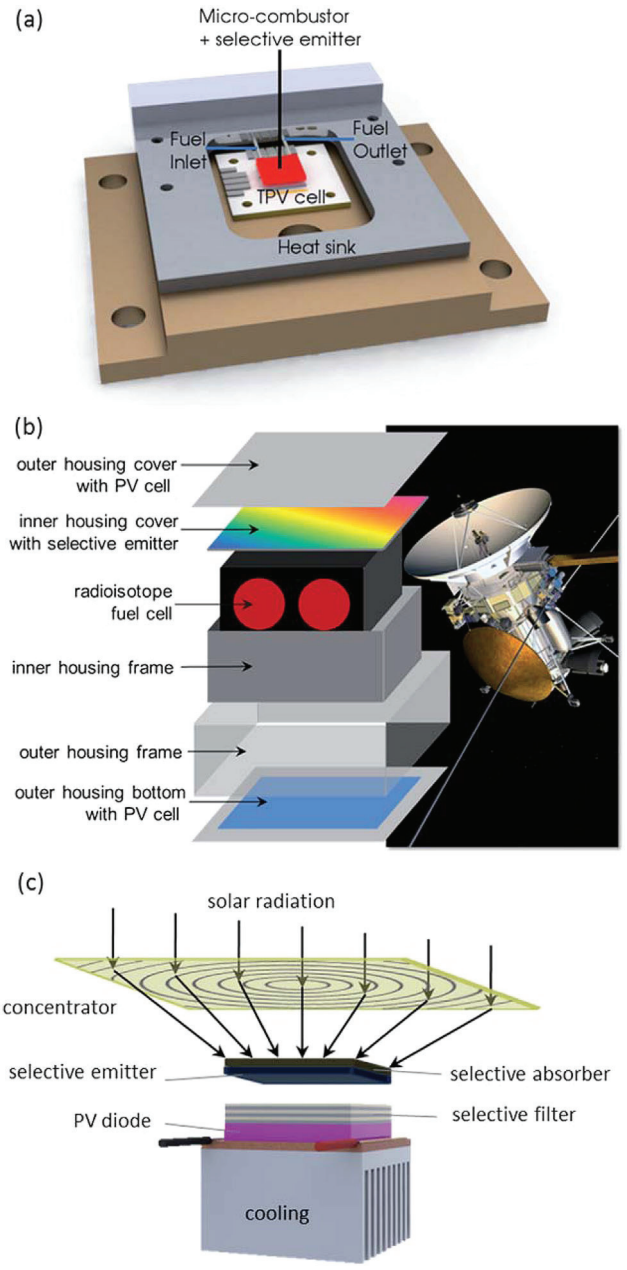

Figure 2 TPV device can use many different heat sources such as (a) combustion using hydrocarbon fuel, (b) heat from radioactive decay, and (c) solar radiation. Reproduced with permission [11]. Copyright 2012, Royal Society of Chemistry.

cooling as the rear-surface is not electrically active [2]. The MIM cells experience increased robustness as the system can be made so the entire cell will not fail if one sub-cell fails when by-pass diodes are included [26].

1.1.2 Filters Spectral control through filters and coatings are used to refine the range of photons incident on the TPV diode. A filter in addition to a selective emitter can aid in emitter temperature maintenence by reflecting unused photons back to the emitter to be absorbed. A good filter should have high transmission of above band gap photons, high reflection of sub-band gap photons, a sharp transmission from reflection to transmission at the band gap energy, and minimal parasitic absorption of energy in the filter [2]. Ideally, any photons with energies far above the band gap, which would increase thermalization or be absorbed too quickly and generate carriers too far from the diode junction, would be reflected as well, but this behavior is difficult to achieve with good sub-band rejection. Filters rely on advanced wave interactions to operate; combined with their tunability based on material choice and design dimensions, many filter technologies are now considered a class of photonic crystal. A more detailed explanation of how photonic crystals work will be discussed in Section 3, but a few specific filter technologies will be briefly described below. A summary of the described filter techniques can be found in Table 1.

One type of filter that is used in TPV systems is a dielectric filter, or a distributed Bragg reflector (DBR) [27, 28], which utilize thin layers of materials with alternating indices of refraction to create interference between incident photons. The materials are selected with the goal of maximizing the transmission of the desired wavelengths and the reflection of all other wavelengths. For a small window of wavelengths, the DBR has high transmittance [29]; however, very long wavelength sub-band gap photons have a low reflection rates [30]. Increasing the number of layers in the filter can reduce this problem, but it can lead to more complicated film growth, increased production costs, and unintentional absorption [31].

Plasma filters are another 1D filter, made of a single layer of heavily doped semiconductor film [32, 33]. The dopant concentration determines the plasma wavelength for the material which establishes the cutoff between reflected and transmitted photons [2]. Common materials for plasma filters are silicon, indium, gallium-arsenide, and transparent conducting oxides (TCOs), such as indium tin oxide, zinc oxide, and cadmium stannate [3]. Absorption around the plasma frequency can lead to a gradual transition between reflectance and transmission wavelength ranges, rather than the preferred sharp changeover [2]. A balance must be struck to minimize above band gap photon absorption and maximize the sub-band gap reflection. Plasma filters can also be combined with interference filters to improve the cutoff sharpness, as well as extend the transmission window into longer wavelengths [34].

Frequency selective surface (FSS) filters increase periodicity to two dimensions with an array of repeating conductive structures. Incident light induces a current in the metallic structures, creating a scatter field that interacts with the incident field to selectively reflect and transmit radiation [35]. The size, shape, and spacing of the pattern influences the photon interactions. Similar structures can also be used to enhance absorption in the diode by increasing light trapping or serving as an antireflection coating (ARC) [36]. As with plasma filters, the FSS generates responses that lack a sharp cutoff on either side of

Table 1 Each form of spectral control has its advantages and disadvantages.

technology	use	structure	response
distributed Bragg reflector	filter	alternating dielectric thin films	high transmission of all frequencies above the cutoff frequency, including high energy photons that contribute to thermalization; low transmission in stop band until long wavelengths
plasma filter	filter	heavily doped semiconductor thin film	no sharp cutoff, so it is difficult to maximize transmission above the band gap and minimize transmission below. Dependent on plasma frequency of the material used
frequency selective surface	filter, antireflection coating	2D metal structure	frequency tunable based on pattern design; high transmission above band gap or high reflectance below, but generally not both
back surface reflector	send photons back through the diode	metal film	above band gap photons get another chance to get absorber. Below band gap photons get set back to emitter; can cause parasitic absorption

This summary includes several of the main approaches and how they can be used in reference to TPV.

the spectrum [31, 35]. Also, ohmic losses due to the conducting layer can increase absorption in the filter [37].

Spectral control does not only include filters; a back surface reflector (BSR) can reflect photons back toward the emitter, giving above band gap photons a second chance to get absorbed and allowing sub-band gap photons to contribute to emitter temperature maintenance [2]. One way to reduce the resulting increased sub-band gap absorption is the use of a hybrid dielectric–metallic BSR. The use of a metallic layer reduces the number of dielectric layers required to achieve high reflectance [38], but it can cause some parasitic photon absorption [2]. Combining a BSR with a front-side filter may still be beneficial enough to outweigh the additional sub-band gap absorption [39]. Application of other surface treatments such as photonic crystals and metamaterials can generate near-field effects that enhance thermal transfer when the gap between the emitter and diode is on the order of 100 nm [40–43].

1.1.3 Emitters Only photons hitting the photodiode produce electric current, so any non-radiative heat coupling between a warm body and the photodiode would be non-convertable and detrimental [2]. The emitter stage of a TPV system (Fig. 1) absorbs heat from an energy source and then emits radiation toward the TPV diode. Use of an emitter stage in the TPV system allows energy from the source transfered via convection, conduction, or radiation, to be turned into usable radiation, making the system energy agnostic in terms of the heat source. The emitter also serves to average the photon flux toward the TPV diode over time, leading to a more constant current.

Emitters are divided into two main categories: broadband and selective emitters. A broadband emitter has a high emissivity over a large range of wavelengths, resulting in a spectral response similar to that of a black body. They are often referred to as "grey bodies" [3] and tend to be made of bulk materials, such as silicon carbide [2]. The use of broadband emitters results in more power being incident on to the TPV diode and more possible power output; however, the broad spectrum of frequencies leads to increased diode heating from thermalization, decreasing device perfromance, and lowering conversion efficiencies [2].

Selective emitters are more popular as modern TPV system components as they only emit a narrow range of wavelengths, resulting in higher conversion efficiencies. Ideally, a selective emitter has an emissivity of zero except for in the narrow desired band, where the emissivity is at or near unity. Regardless of the heat source, any selective emitter will only radiate in its characteristic spectrum. A narrow emission spectrum just above the band gap energy would result in a high conversion efficiency nearing the external quantum efficiency of the photodiode in the limiting case. However, the narrow frequency band emission results in less power. Thus, a balance between efficiency and power must be achieved to maximize the benefit of a selective emitter for a given application.

1.2 Thermal radiation A perfectly radiating body, a blackbody, has an emissivity of 1 at all wavelengths and the power output for the blackbody at any given temperature can be calculated using Planck's law [44, 45]. Other objects emit a percentage of the blackbody curve depending on their emissivity at a given wavelength, but the power output scales as the object's temperature is increased. To make the best use of the available power, the peak of a selective emitter spectrum should also occur at the peak of the blackbody curve. The peak wavelength of a radiating blackbody can be calculated using Wien's law [45]. For the highest efficiency, the emitter spectrum peak should occur slightly above the band gap of the diode in use. For example, to match the band gap of presently available GaSb TPV

diodes and optimize the output based on the blackbody curve, a selective emitter needs to operate at 1400 °C. The designed emitter must be able to withstand these high temperatures.

According to Kirchhoff's law of thermal radiation, at equalibrium the emissivity of an object is equal to the absorptivity of that object [46]. This relationship is taken advantage of frequently in the development of emitters for any application. absorption measurements have historically been the first-stage in understanding optical properties of a material due to the relative ease by which these measurements can be done. Heating a sample over 1000 K to test emission brings in new safety concerns and the potential for damaging the sample. High temperature testing is particularly difficult for many nanostructured materials as the structures experience degredation below the melting point. Testing first for absorption and then for emission allows the separation of optical and mechanical properties of a given sample, providing more information for future designs.

2 Fixed spectrum emitters

2.1 Plasma emitters Plasmas emitters utilize electrons dropping from a higher energy state to a lower one in order to create a stream of photons at a given energy [3]. Though the majority of plasmas today utilize an applied voltage or current in order to start, plasmas can also be generated using high temperature sources. Thermionic emission from a hot metal surface increases the denstiy of energetic electrons in a volume. If that volume contains a gas such as helium, argon, or cesium, the additional electrons can prompt enough ionization events that a plasma will form [47]. The temperatures required for sufficient emission to strike the plasma are typically higher than 2000 °C [48, 49].

The characteristic emission peaks of a cesium plasma, as shown in Fig. 3, corresponds to the band gaps of gallium arsenide and indium phosphide [50, 51]. The radiation efficiency of the reported cesium plasma reached greater than 70% for certain atomic densities, with the optimal radiation efficiency occurring when the neutral atom density was on the order of $10^{21}/m^3$ [51]. Unfortunately, this high efficiency is offset by a high operating temperature and low power output. In order to emit the desired wavelength and number of photons, the plasma has to obtain a temperature between 2000 and 3000 K [51]. The power output from the PV cell in the reported system is low due to the low density of the cesium plasma. Manipulation of the plasma conditions such as density and temperature can cause peak broadening [50] due to Doppler and Stark effects, excitation transfer, or other mechanisms [52]. This broadening can lead to more power output due to the presence of additional photons, but the wider range of frequencies can impact overall efficiency.

Recent work has theoretically shown the utility of dusty microplasmas as a radiation source [53]. A microplasma is a non-equilibrium plasma less than 1 mm in any dimension that operates at atmospheric pressures [54]. Small particles, or dust, introduced to such a plasma become negatively charged, allowing suspension in the electric field generated by the plasma [55]. The particles are heated through collisions with plasma particles, prompting thermal emission of photons according to the emissivity properties of the dust material. Usage of ceramic oxides such as alumina and aluminum oxynitride will generate selective peaks in the mid-IR [53]. Preliminary explorations into the effect of particle size has shown varied peak intensity and selectivity as the size is increased, as shown in Fig. 4. Additional research on other materials and grain sizes is needed in order to optimize a microplasma device for use as a selective emitter.

2.2 Rare earth materials As early as the 1930s, the Lathanides, or rare earth metals, were shown to have unique absorption and emission spectra [56]. It was not until 1972 that the potential for use as a selective emitter was recognized and the emission spectra specifically studied [6].

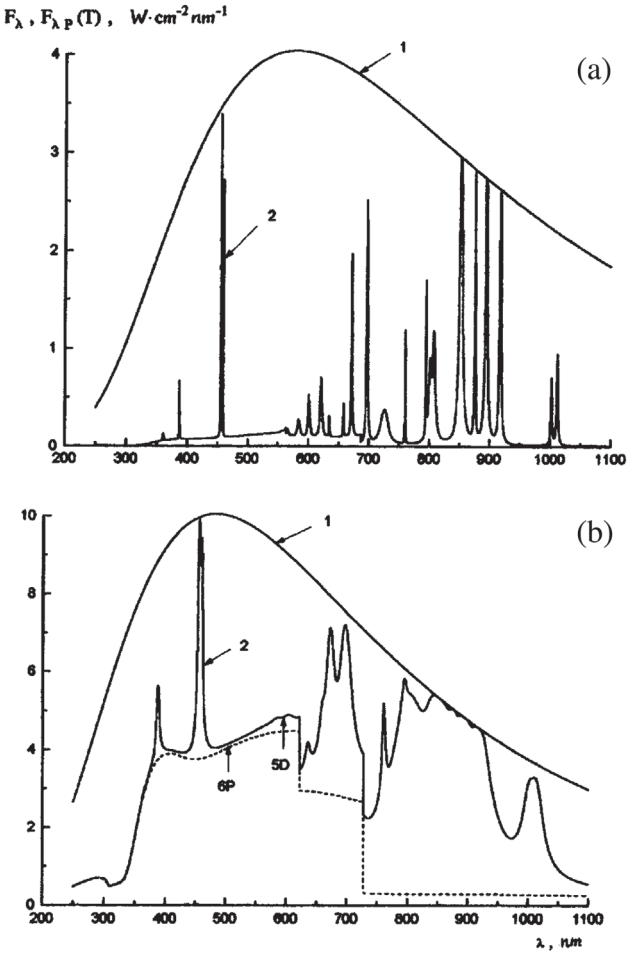

Figure 3 Radiation from a cesium plasma can change slightly based on the plasma conditions, but the main peaks remain at the same wavelengths. Shown are the spectra from a plasma column with $R = 2.5$ mm: (1) $F_{\lambda P}(T)$, (2) F_λ; (a) $n = -8 \times 10^{16}$ cm^{-3}, $T = 5000$ K, (b) $n = 8 \times 10^{17}$ cm^{-3}, $T = 6000$ K. Reproduced with permission [50]. Copyright 1997, American Institute of Physics.

Since then, rare earth oxides have been shown to be a promising source of radiation for TPV [57] and other applications [58, 59]. Oxides are the most commonly used rare earth compound, particularly for high temperature applications, as they are the most thermodynamically stable form [60]. Incorporation of rare earth ions into host materials has also garnered much interest as a way to combine the spectral performance of the lanthanides with high thermal performance of other ceramics and crystals [61].

2.2.1 Emission mechanism Photon emission from a rare earth metal comes from a high energy electron dropping down to a lower energy state. The unique atomic structure of the lanthanides means emission in the wavelengths specific to each metal is preserved even when a lanthanide atom is bonded to another compound. Moving toward the right on the periodic table from cerium to lutetium shows gradual filling of the 4f orbital, with the complete configuration of $[Xe]6s^2 4f^n 5d^m$ [60]. This orbital has a higher energy than the 5s and 5p orbitals, but a smaller radius. The larger radii of the 5s and 5p orbitals means these filled states shield the 4f electrons from their environment, as seen in Fig. 5. As these states are effectively isolated from their environment, the 4f energies are minimally impacted by the surrounding crystal structure while the more exposed 5d levels are heavily influenced by the crystal fields of its surroundings [60]. The 4f-4f transitions remain consistent resulting in narrow, well defined peaks, but 4f–5d transitions are dependent on the surrounding crystal structure and symmetry, resulting in broader emission peaks [60].

Though the emission peak position is independent of the host material, the strength of this peak can be influenced by the surrounding crystal. Non-radiative relaxation of excited electrons can depopulate the desired transition levels, reducing the intensity of the corresponding spectral peak. One theory on how to reduce this effect is to dope the host material with multiple rare earth elements, such as Yb and Er. Multiple doping offsets the ions' energy levels and can prompt more phonon-assisted energy transfer, increasing the coupling of emitting ions with the phonon subsystem of the emitter [63]. More recent simulations focused on the crystal structure by using a point-charge model to calculate the crystal field parameters for an amorphous phase of erbium oxide in an alumina matrix and the erbium aluminum garnet structure (EAG) [64]. The model accurately tracks experimental data for an EAG sample at various temperatures, as seen in Fig. 6. Comparison to experimental data confirmed the non-radiative

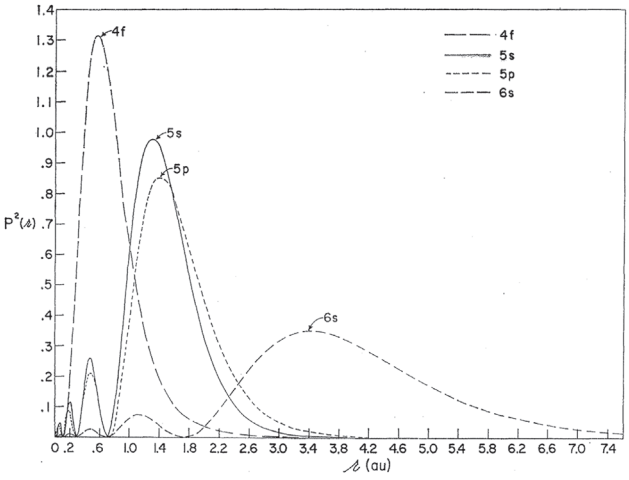

Figure 5 Square of the radial wave functions for the 4f, 5s, 5p, and 6s orbitals of Gd. As the filling order is 5s, 4d, 5p, 6s, 4f, an unfilled 4f orbital is protected from the surrounding crystal by the filled 5s, 5p, and 6s orbitals further from the ion. Reproduced with permission [62]. Copyright 1962, American Physical Society.

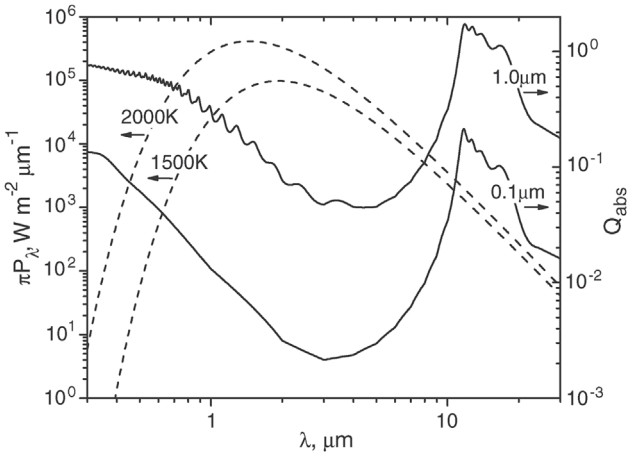

Figure 4 The absorption efficiency (Q_{abs}) of dusty plasma changes with grain size ($R = 0.1$ and 1 μm). Overlaid are graphs of the Planck function P_λ versus λ for $T = 1500$ and 2000 K for comparison on the peak wavelengths. Reproduced with permission [53]. Copyright 2010, IEEE.

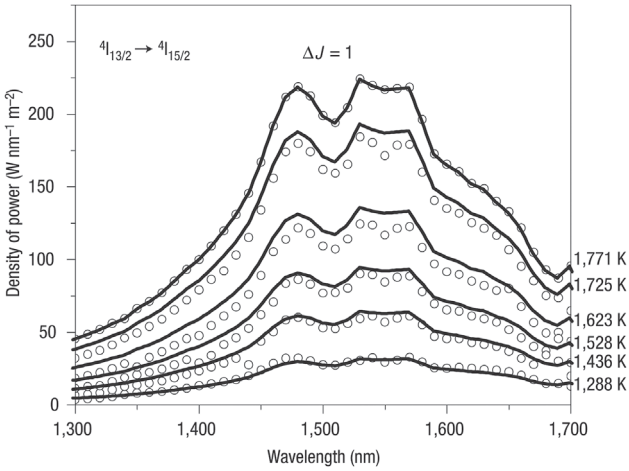

Figure 6 Experimental high temperature emission spectra of a crystalline EAG sample that was sintered at 1400 °C (solid line) compared to the theoretical prediction (circles). Reproduced with permission [64]. Copyright 2004, Nature.

decay route was more efficient in the amorphous samples and equally likely compared to radiative events in the garnet structure [64]. This means the garnet form offers more promise in terms of emitter efficiency than an amorphous rare earth material.

2.2.2 Structures and materials Rare earth oxides are of interest for high temperature applications due to their thermodynamic stability [65, 66]. A comparison of oxide emitter materials suitable for TPV, including the transition metals Ni and Co that are often used in a similar fashion, can be seen in Table 2 with the PV and TPV material band gaps they can be matched to. Erbium oxide is well suited to TPV as its spectral peak appears at 1.54 μm (0.81 eV), slightly higher than the band gaps of Ge and GaSb. Several host materials and fabrication methods have been studied [67, 68]. A common early TPV emitter design is the mantle, a cylindrical or slightly conical structure named after the gas lantern component that it resembles, which allows for radial emission of photons. The mantle is surrounded by TPV cells, as seen in Fig. 7. An emitter fabricated from Y_2O_3 and coated with Er_2O_3 was tested at 1680 K, resulting in a peak emissivity of 0.82 at the wavelength 1.55 μm [70]. Similar results have been obtained for a disk emitter by plasma-coating Er_2O_3 onto a SiC substrate [71]. However, the strength of the selective peak compared to the SiC background emission was dependent on the thickness of the erbium layer, with emissivity approaching gray-body behavior for thicknesses less than 118 μm [71]. This matches well with previous theoretical analysis that the emission efficiency of a rare earth oxide thin film is tied to its thickness [72, 73].

Use of Er as a dopant or in a suspension has been the focus of research since the early 2000s. Fabrication methods for rare earth ions in a suspension vary from ceramic slurries in molds [67] to sol–gel preparation [68] to electrospun nanofibers [75, 76]. In all cases, the intent was to improve the thermal and mechanical characteristics of the emitter while still taking advantage of the Er emission spectrum. Sol–gel preparation using a silica-based binder resulted in the most improvement in terms of modulus of rupture and thermal shock resistance [68]. Direct incorporation into a crystal structure as a dopant has largely made use of the

Table 2 Energy and wavelength of the primary emission peak for common rare earth and transition metal oxides along potential photovoltaic cell material matches.

material	energy (eV)	wavelength (μm)	matched PV material
Yb_2O_2	1.27 [10]	0.98	Si
NiO	0.88 [72]	1.41	Ge, GaSb, InGaAs
Co_3O_4	0.84 [72]	1.48	Ge, GaSb, InGaAs
Er_2O_3	0.81 [10]	1.54	Ge, GaSb, InGaAs
Ho_2O_3	0.62 [73]	1.85	InGaAsSb
Nd_2O_3	0.52 [73]	2.38	InPAsSb

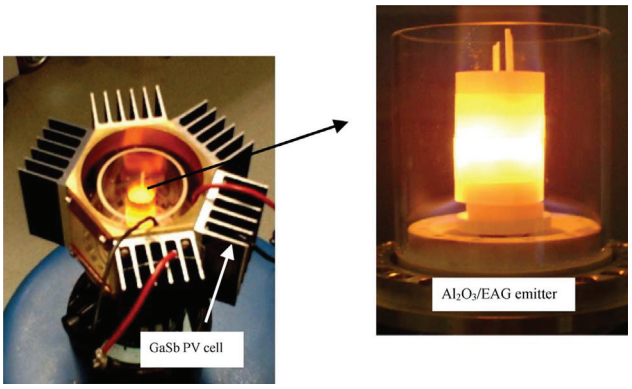

Figure 7 Complete view (left) and interior (right) of a single-burner TPV test rig utilizing a Al_2O_3/EAG eutectic ceramic mantle as an emitter. Reproduced with permission [79]. Copyright 2005, Elsevier.

yttrium aluminum garnet (YAG) crystal [74, 77–79] due to its high melting point and low emissivity in the near-infrared (NIR). Early testing made use of bulk crystalline samples [74], resulting in the emission spectrum shown in Fig. 8, but more recent efforts have used powdered ErAG, or erbium-doped YAG, in sol–gel [77] or plasma-spray coating [79] preparations. Erbium has also been integrated into a crystal through the use of $Al_2O_3/Er_3Al_5O_{12}$ eutectic ceramics [79], with the emission spectrum shown in Fig. 9. The eutectic ceramic contains single-crystal microstructures of its constituent materials that merge together without grain boundaries, which results in excellent high-temperature performance in terms of strength, oxidation resistance, and thermal stability. The $Al_2O_3/Er_3Al_5O_{12}$ compound was found to have similar emission efficiency compared to an ErAG single crystal but with improved mechanical strength and thermal stability [69].

Though Er has the best positioned characteristic peak to match with common TPV materials, emitters made from other elements have also been tested. Ytterbium, Yb, can

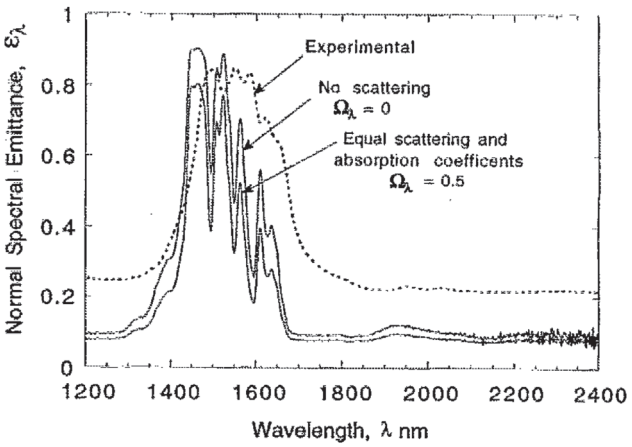

Figure 8 Comparison of two theoretical models and experimental emittance for 40% Er-YAG. Reproduced with permission [74]. Copyright 1994, AIP Publishing.

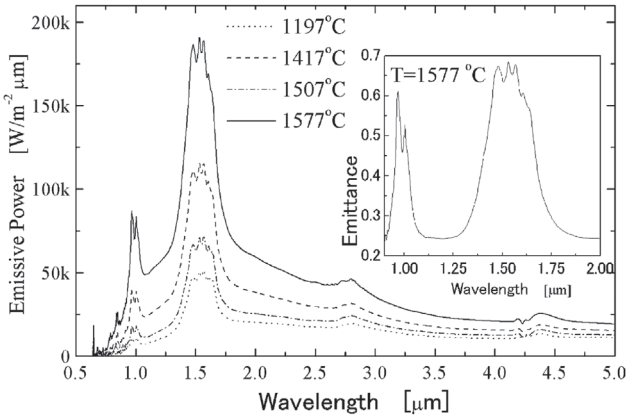

Figure 9 Spectral emissive power at a range of temperatures of the Al_2O_3/EAG eutectic ceramics. Inset is the emittance near the primary peaks. Reproduced with permission [69]. Copyright 2005, Elsevier.

emit photons that are well matched to the band gap of silicon, but it can also supply enough energy to work with other TPV cells. A mantle-style emitter made with Yb_2O_3 was compared to the previously mentioned Er_2O_3 mantle, achieving an emissivity of 0.85 at a photon energy of 1.27 eV [70]. The emission spectra for each of these mantles was applied to models of silicon- and germanium-based photocells and the resulting efficiencies compared to that achieved through solar irradiation. The results can be seen in Table 3. The Yb_2O_3 mantle improved the efficiency of both cells compared to solar irradiation, but the silicon cell/ Yb_2O_3 mantle and germanium cell/ Er_2O_3 cell combinations attained the highest efficiencies [70].

Use of Yb as a dopant has been explored using a wide variety of host materials. Compounds with as low as 10 mol.% showed the characteristic emission peak of Yb, though the peak tended to be lower in intensity and broader than that produced by higher percentages [80]. YbAG, yttrium aluminum garnet, along with $YbNbO_4$ and $Y_{1-x}Yb_xO_{1.5}$, proved to be the best candidates as selective emitters for their high ratio of peak intensity to host material background emission [80]. Figure 10 shows a comparison of the bulk Yb_2O_3 emission to that of Yb-doped YAG. The characteristic peak is strong in the Yb:YAG, though the maximum emittance is not quite as high as with bulk Yb_2O_3.

Though they are not considered rare earth metals, the transition metals nickel and cobalt have been used in a similar fashion to create selective emitters. Low mole fractions ranging from 1 to 4% of NiO and Co_3O_4 were

Table 3 Efficiencies of two modelled photocells under different irradiation [65].

cell	η_{solar} (%)	η_{Yb2O3} (%)	η_{Er2O3} (%)	η_{max} (%)
Si	19	30	8	35
Ge	7	14	18	21

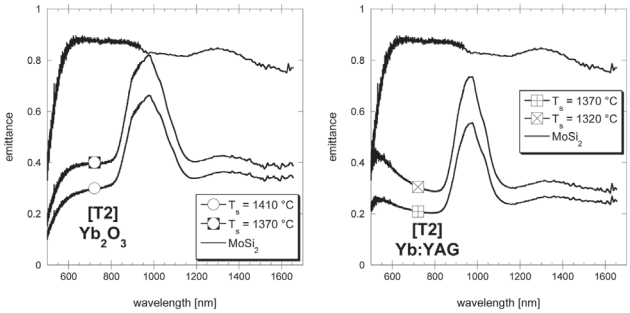

Figure 10 Measured emittance of plasma-sprayed Yb_2O_3 (left) and Yb:YAG (right) on a $MoSi_2$ substrate. Reproduced with permission [79]. Copyright 2007, AIP Publishing.

incorporated into a MgO host. Electronic transitions between the host material and the partially empty bands of the dopant ions resulted in selective peaks at 1.41 μm for NiO-doped MgO and 1.48 μm for Co_3O_4-doped MgO when the material is thermally stimulated between 1300 and 1400 °C [82]. The NiO-doped emitter's power spectrum (Fig. 11) outperforms a blackbody with the same total power at wavelengths less than 2 μm, which is a more useful wavelength range for photodiode conversion [81].

3 Tunable spectrum emitters The previous emitters are good candidates for TPV applications due to their highly selective peaks, but the peak wavelengths are linked to the atomic structure of the materials used and cannot be shifted. The addition of other compounds can broaden the overall peak [61], increasing the power output of the emitter, but the spectral position in terms of wavelength remains the same.

New techniques in nanofabrication and an increased understanding of the way electromagnetic waves interact with materials has led to the development of spectral engineering, or the controlled manipulation of a device's constituent materials or spatial design to generate a desired absorption/emission spectrum. Though it was first mentioned off-hand in 1992 in reference to adjusting a potential well in order to change the quantum allowed and forbidden state spectra [83], it was not until 2001 that "spectral engineering" was used to correlate physical differences between nanostructures and the resulting changes in their optical spectra [84]. Today, plasmonic devices, generally in the form of photonic crystals and metamaterials, offer the best solution for selective emitters in terms of customizing their spectrum for specific applications.

3.1 Photonic crystals Photonic crystals (PhCs) offer a more engineerable option of selective emitter than what is available naturally [36, 85, 86]. A photonic crystal is an array of multiple materials that repeats in one, two, or three dimensions [87]. The dimensions of repetition determine how many planes of photonic response will be induced while the size of the repeated geometries will change what wavelength is affected [87]. PhC behavior was shown as

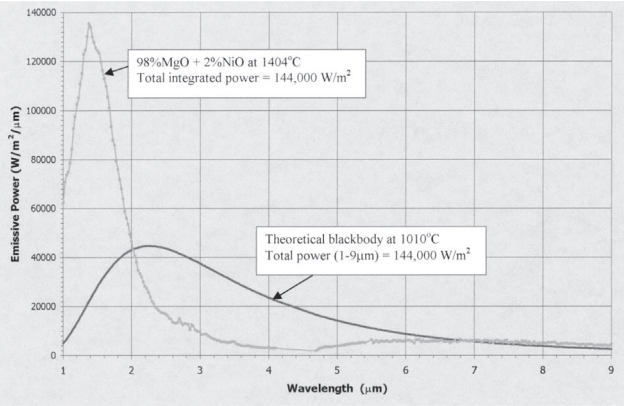

Figure 11 Emissive power spectrum from a 2 wt.% NiO-doped MgO emitter at 1404 °C compared to the theoretical blackbody spectrum at 1010 °C. The total power from each radiating body is the same, but the spectrum from the NiO-doped emitter is more useful for conversion with TPV technologies. Reproduced with permission [81]. Copyright 2001, Elsevier.

early as 1987 [88, 89], but application to high-temperature cases such as TPV did not begin until the turn of the millenium [90, 91]. Metallic photonic crystals utilizing tungsten [92] or tantalum [11] show promise as high temperature emitters, but in many cases require special packaging such as maintenance of an inert atmosphere. The sharp turn-on frequency induced by these devices reduces the number of low energy photons that hit the TPV diode [11]. However, many of them maintain a high emissivity of high energy photon at frequencies above the turn on frequency [11]. The relaxation of these high energy photons can lead to parasitic device heating and reduced conversion efficiency. Also, difficulties in manufacturing nanostructures using tungsten can limit the potential applications [11].

3.1.1 Emission mechanism Unlike the previous emission methods, the characteristic spectra of photonic crystals are not based solely on the atomic structure of its constituent materials. Rather, selective emission occurs due to complex optical effects. When light is incident on a multilayer film made of materials with different permittivities, reflection and interference occurs between the layers if the wavelength is on the order of the layer thickness. This interference results in forbidden photon momentum vectors, which appear as a photonic band gap in the wave vector diagram. The allowed states are predicted by the Bloch wave vectors that lie in the Brillouin zone. PhC behavior is often discussed in terms of the photonic band gap as the concept is easily translated to two and three dimensional structures.

Manipulating the PhC design can elicit many unique effects in these structures, including: surface plasmon resonance [93–95], resonant cavity enhancement [96, 97], Wood's anomaly [98, 99], Bragg reflection [100, 101], and/or modification of the photonic density of states [102, 103]. The particular mode used for emission varies based on the design in use. In some cases, several resonant modes appear at different wavelengths, resulting in multiple emission peaks in the final spectrum [104]. The generated resonant modes can also be used for device enhancement. For example, surface phonon polariton coupling can greatly enhance near-field energy transfer in the IR when using polar materials. The heat transfer coefficient in SiO_2 increased by three orders of magnitude when the two surfaces were separated by a 30 nm gap [105]. However, application to PhC structures shows a trade-off between near-field enhancement and spectral selectivity [106].

Discussion of the particular optical modes generated for a given design will be included in the subsection on structures. For more detailed explanations of photonic crystals designs and their applications in photonic devices, see the included references [87, 107].

3.1.2 Modeling and theory Modeling of PhCs requires calculating the transmission and reflectance coefficients of the potential structure. Some groups employ the transfer matrix method (TMM) which calculates the transmission and reflection for a small "cell" of the structure and then couples those fields to the surrounding cells. The final matrix relates the incoming fields to the outgoing fields [108]. Application of Green's dyadic in a momentum space to the TMM has led to a derivation of Kirchhoff's law for PhCs and was used to look at coherence in emission from a SiC grating [109]. Rigorous coupled-wave analysis (RCWA) [110] is a fast calculation method for predicting the effects of diffraction on a planar grating [111, 112]. It solves Maxwell's equations by expanding the fields in terms of Floquet harmonics and adhering to the given boundary conditions [113]. What makes this method computationally light is that it uses a coefficient matrix that contains the diffracted wave propagation and coupling information and then calculates the eigenvalues and eigenvectors before constructing the linear equation system [110]. Other direct analysis methods include photonic band gap and density of states calculations [114, 115], direct calculation of the transmission-absorption spectral profile [116], and Q matching of resonances [112]. Focusing on the flow of thermal radiation is another modeling approach that may offer benefits over other density of states calculations [118].

A common tool, and a more brute force method, used when modeling electromagnetic field interactions in complex structures is the finite-difference time-domain (FDTD) technique [117, 118]. The FDTD method takes the differiential form of two of Maxwell's equations and solves them in discrete time steps at predetermined spatial points in the object of interest. By using discrete time intervals of a known duration and a known spatial distribution, Maxwell's equations will give the unknown electric and magnetic fields that will be present in the future in terms of known fields that occurred in the past [119]. Solving these equations will make those future fields known, allowing progression to another step into the future.

However, simultaneously solving these equations at the same point in time can be very difficult and messy. To streamline the process and make the technique more computer-simulation friendly, an offset coordinate system, known as the Yee square, was adopted [119]. The electric field solve points in 3D space are offset from the magnetic field solve points by one-half of a step in space and in time, allowing the electric field and magnetic field to be established separately at different points until the whole timespan of interest has been calculated. The standard FDTD equations can be modified to include additional quantities such as thermal fluctuations [120] or use different computational approaches such as pervasive interpolation [121].

Application of these models to PhCs has shown that Kirchhoff's law should hold true when at equilibrium [109, 114, 120, 123] though there is conflicting information on whether the blackbody limit via Planck's law still holds. Calculation says it should for both equilibrium and non-equilibrium [106, 120] cases, but some controversial results via both modeling, shown in Fig. 12, and experimentation, shown in Fig. 13, report that PhCs can exceed the blackbody limit. In terms of modeling, it has been noted that this excess could be lost in practice due to non-radiative losses and unaccounted for coupling effects between the PhC and the blackbody source [122]. Theoretical calculations using infinite PhCs rather than devices of a finite size could also contribute to this [114]. Corroboration from experimental data is less clear, as inconsistent reporting of device temperatures make it difficult to compare to the corresponding blackbody curve [124]. However, there is agreement that the PhC increases power density in the wavelength range of interest and overall can improve the optical-electric conversion efficiency of TPV diodes compared to just using a blackbody [91, 125–127].

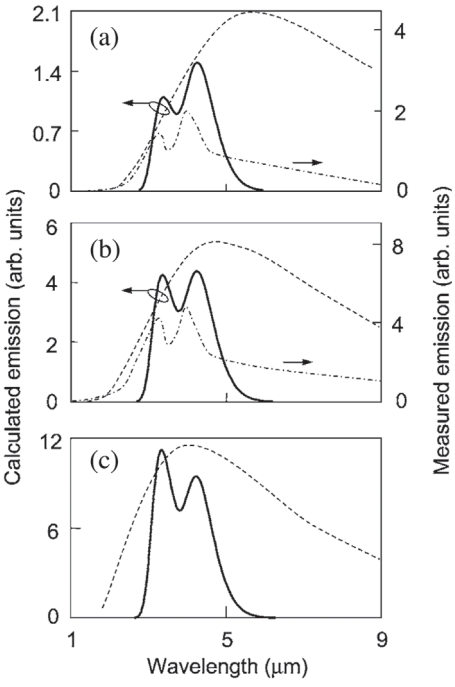

Figure 12 Theoretical calculations of a lossy photonic-crystal's emission (solid curves) show the possibility of outperforming a blackbody (dashed curves). (a) $T = 500$ K, (b) 600 K, and (c) 700 K. Reproduced with permission [122]. Copyright 2005, American Physical Society.

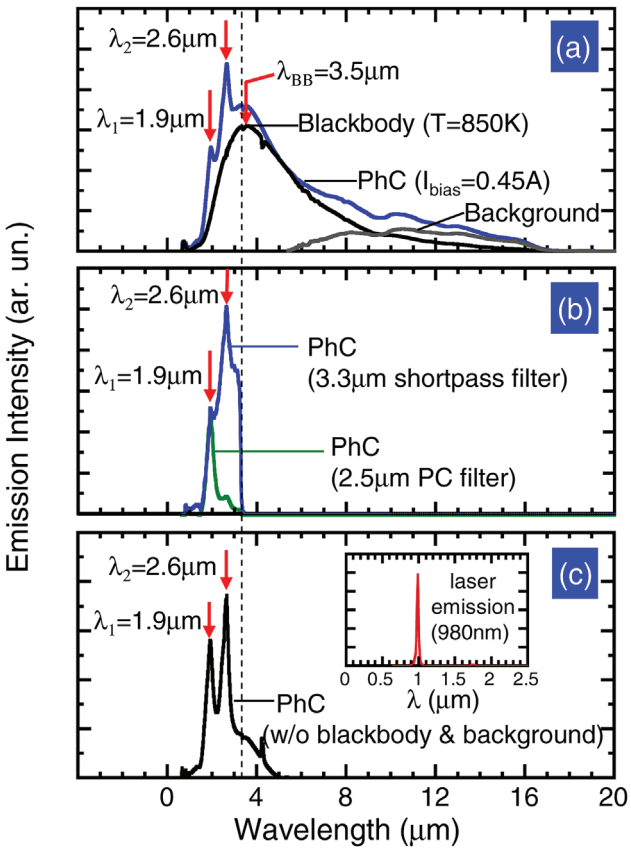

Figure 13 Thermal emission spectra measured from a PhC sample, (a) at $I_{bias} = 0.45$ A compared to a blackbody source at $T = 850$ K, (b) at 0.45 A bias with a $\lambda = 3.5$ μm shortpass filter (blue curve, doublet) and $\lambda = 2.5$ μm PhC filter (green curve, singlet), and (c) at 0.45 A bias without the blackbody and background emission. Reproduced with permission [124]. Copyright 2013, OSA Publishing.

3.1.3 Structures Photonic crystals can be made with symmetry in one, two, or three dimensions. Though 2D structures are the most common design for TPV applications due to their preferential emission along the z-axis, a useful feature due to the TPV system setup and resulting cavity geometry, all three options have been explored. In general, the difficulty of fabrication increases as the number of dimensions increases, so novel fabrication techniques have also received attention [128–130]. Though the following devices focus on emission characteristics, similar PhC structures have also been used as an enhancement for TPV [85], light emitting diodes [131], and sensors [132–134].

Temperature testing of PhC emitters has reached temperatures as high as 1200 K [126, 135]. However, testing generally occurs under vacuum or in an argon atmosphere. Although vacuum and inert atmosphere testing has been used to provide material performance information, such as demonstrating improved stability of Ta nanostructures when a hafnium oxide coating is used [126, 136, 137], such an atmosphere is impractical for use in most TPV systems. Maintaining a prepackaged vacuum environment like what would be found in a production device is difficult with both high and fluctuating operating temperatures. Relying on the evacuated atmosphere in space applications, where the vacuum is a part of the natural environment rather than artificially created, would also be problematic. Such devices would be put in contact with the general purpose heat source, a radioactive decay-based heat source,prior to launch [138], meaning the device would still experience high temperatures in a mixed-gas atmosphere. Further testing in an oxygenated atmosphere is needed to show the practicality of PhCs as high-temperature emitters in a TPV system. The main PhC designs along with their highest achieved temperatures in different operating environments are summarized in Table 4.

Though 1D PhCs are most commonly made of dielectric materials and used as filters [125, 144–146], a few designs have been explored for their utility as emitters. A purely dielectric PhC has been used as the selective emitter in a microthermophotovoltaic system. The Si and SiO_2 stack is used to shape the emission from the graybody Si [147]. One approach is to use a plane of metal, commonly silver, or another emitting material such as SiC with thin, alternating layers of dielectrics forming a PhC [97, 143, 148, 149]. Figure 14 shows a side view of this structure with the square of the electric field both with and without an excited surface wave. Use of a polar material such as SiC on top of the dielectric PhC allows a cavity resonance to occur, enabling an emission peak in the PhC stop band where no energy can be transmitted [149]. Other emission modes such as the Brewster mode, which only occurs with p-polarized light at large incidence angles [149], create additional peaks in the overall spectrum with this design. A similar cavity resonance effect can be achieved with a thick layer of dielectric between the metal layer and PhC. With this design, the standing wave occurs in the dielectric cavity and the metallic layer acts as mirror and source of thermal radiation [97]. Use of a grating rather than a thin film of metal achieves the same result [149].

Metallic layers are most commonly used as high quality reflectors, but the inclusion of thin layers on the order of the skin depth [150] in a PhC can broaden the photonic stop band [151] and allow PhCs that operate in the NIR and optical wavelengths [152]. Silver and tungsten have been explored through simulation [150] and also experimentally [104] as components of PhC emitters. In both cases, emittance at the desired wavelength was greatly improved compared to the response of a plain metallic film. Unlike the previously mentioned designs, the emission mechanisms for the tungsten/dielectric peaks were attributed to surface plasmon-polariton excitation, gap plasmon-polariton propagation, and magnetic polariton excitation for the three peaks that appeared [104]. Theoretically calculated efficiencies for the tungsten emitter were higher than 50% when the emitter was at a temperature of 1600 K or higher [104].

Cavity resonance has also been leveraged with metallodielectric PhCs to create selective emitters through the fabrication of a Fabry–Pérot cavity, a dielectric layer with highly reflective surfaces on both sides. A silver base with 2 μm of SiO_2 and 15 nm of Ag was shown to have several sharp emissivity peaks in the NIR with a wavelength-dependent angular distribution [143]. More recent work has focused on enhancing the tunneling effects through the thin top layer and reduced the Ag thickness to 1 or 2 nm. Adjusting the thickness of the silicon cavity shifts the emissivity peak location, while tuning the Ag top layer thickness changes the FWHM [139].

Increasing the PhC complexity to two dimensions allows structures with more customization options and, more importantly, increased emission coupling in the z-direction. The most common design utilizes holes in a triangular lattice. This design gained popularity as it combines the effects of

Table 4 Photonic crystals come in many designs and materials.

dimensions of symmetry	pattern	materials	highest non-destructive temperature
1	repeating dielectric with single or repeating metal or ceramic layer	Si,SiO_2, Ag, W, SiC	room temperature [104]
1	Fabry–Pérot resonant cavity	Ag with SiO_2 or Si middle layer	100 °C in nitrogen [139]
2	rods	W, Ta, W-Ta alloy, GaAs, VO_2	1000 °C in argon [126]
2	grating	W, Au, GaP, TiN, steel, metallized plastic, GaAs MQW, Si	200 °C in air [140]
3	woodpile	Cu, Ag, Au, W	620 °C in argon [141]
3	inverse opal	Si, C, or metal scaffold, coated in Pt, Mo, or W	1000 °C in forming gas [142]

Though materials such as tungsten and tantalum offer promise as high temperature devices, recorded experimental temperatures vary widely and often occur in an inert gas.

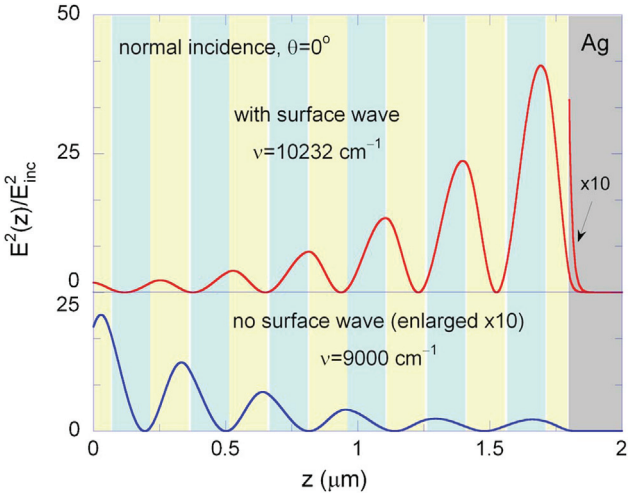

Figure 14 When a surface wave is excited, resonance occurs at the interface between the dielectric PhC and the Ag layer, as seen by the electric field (square and normalized by the incident electric field here) in the top panel. Without a surface wave, this resonance does not appear. Reproduced with permission [143]. Copyright 2006, AIP Publishing.

dielectric rod and dielectric vein PhCs, creating a complete photonic band gap for multiple polarizations [87]. Early works used silicon as the primary material with air serving as the secondary dielectric in the holes [90, 125, 153]. Focus on high-temperature performance led to PhCs fabricated in tungsten (W) [92, 135, 154–156], tantalum (Ta) [126, 136, 157–159], and a tantalum-tungsten alloy [137]. Recently, research has turned to unusual materials such as GaAs [160] and vanadium dioxide [161]. Fabrication consists of lithography to establish the pattern and etching via chemical etchants or reactive ion etching. Design elements include the depth and diameter of the holes as well as the hole spacing. Examples of fabricated W PhCs with different radii and depths are shown in Fig. 15, along with their measured emittances compared to a flat W film in Fig. 16. Recent conference results have confirmed these results [162, 163].

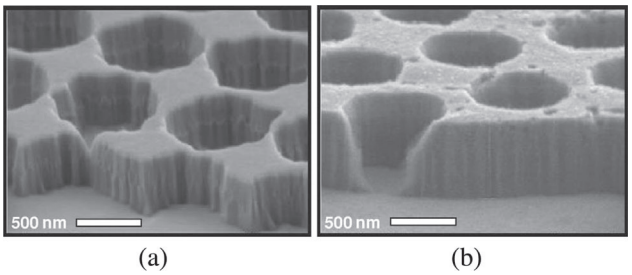

Figure 15 A common PhC emitter design uses air rods in another material, in this case W, to generate the desired spectrum. The spectra can be altered by changing the rod radius and spacing. (a) $r = 450$ nm, $d = 560$ nm, $a = 1$ μm and (b) $r = 390$ nm, $d = 600$ nm, $a = 1$ μm. Reproduced with permission [156]. Copyright 2008, AIP Publishing.

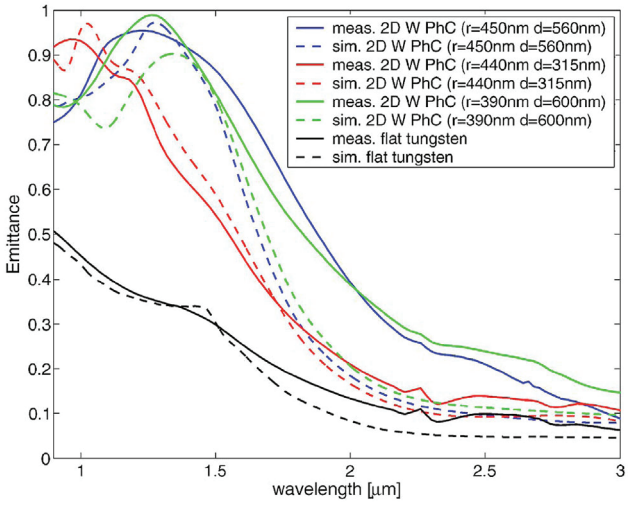

Figure 16 A comparison of the emittance spectra of three 2D W PhC designs (experimental and simulated) to a flat W film. Reproduced with permission [156]. Copyright 2008, AIP Publishing.

Emission from the air column structures comes from constructive interference of evanescent waves at the structure surface, with control of the resonant frequency coming from the hole spacing [164]. Coupling of the surface plasmon modes to light allows propagation in all planes perpendicular to the crystal surface [109] The propagation path of these modes is why the hole-array design has a complete band gap across all polarizations. Isolated areas of high permittivity generate nodes in the high frequency TM modes, while veins of high permittivity does the same for TE modes. Strategically placed holes create effectively isolated rods connected by thin veins [87]. The combination of these effects generates a band gap for TE and TM polarized light, as seen in Fig. 17. This phenomena can also be thought of as cavity resonances in the PhC leading to allowed and forbidden modes [166].

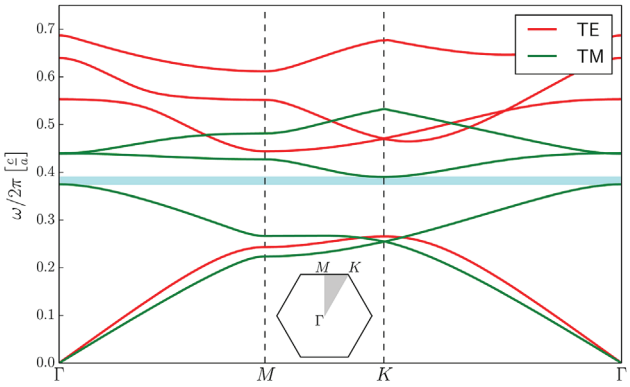

Figure 17 By combining design elements of rod PhCs and mesh or vein PhCs, air rods in a triangular lattice can create a complete photonic band gap. Reproduced with permission [165]. Copyright 2015, OSA Publishing.

The use of gratings as 2D PhCs has also largely focused on tungsten as the primary material [98, 111, 118, 167–170]. Other work has used a gold grating on a 1D dielectric PhC [171], gallium phosphide [172], steel (Fig. 18) [140], titanium nitride [173], metalized plastic [174], and GaAs-based multiple quantum wells [175]. These structures also utilize surface plasmon-polari ton and cavity resonances to emit, though the response is more heavily polarization dependent [118]. Deep gratings can also induce localized magnetic polaritons that enhance thermal emission [169, 176]. Broader peaks can be generated by creating complex gratings, or combining two binary gratings into a single pattern [98]. Using a thin layer of SiO_2 in the middle of a W grating also generates broader peaks with a large-polarization dependent response, as seen in Fig. 19 [167]. Introducing doped silicon as the material for the complex grating design can also generate a broad peak but with decreased incident angle sensitivity [177]. Use of the genetic algorithm, an iterative process that adjusts the design parameters to maximize the emittance at the wavelength of choice, helps to automate the design optimization process [111].

Unlike the 2D designs which use the same fabrication technique regardless of ultimate design, each 3D PhC has a different fabrication method for the main structure types. The resulting structures more closely mimic a crystal lattice. In fact, the primary designs used for emitter applications have a face-centered cubic (fcc) lattice structure. The fcc lattice is ideal for this application as the nearly spherical Brillouin zone and axis-independent spatial periodicity leads to band gaps in three dimensions [87, 88].

One of the main designs used in emitter applications is the haystack, also known as the woodpile or Lincoln Log pattern. This pattern consists of metallic bars with each layer laid perpendicular to the one before it, with parallel layers shifted by half a period, as seen in Fig. 20. In general, fabrication occurs layer by layer using e-beam lithography and traditional metal deposition techniques [178]. A direct write process using a laser to expose the pattern has also been developed; in this method, the developed resist is annealed to create a silica lattice and then coated in the desired metal [141]. Most recently, a top down technique has been developed that will create an angled haystack. Use of an angled metal plate manipulates the ion sheath formed when using a reactive ion etch, allowing the incident ions to approach the sample surface off-normal [179]. Room temperature samples and theory explorations have utilized metals such as copper [178, 180], silver [180], and gold [180], but high-temperature efforts have focused on tungsten [91, 124, 141]. When using tungsten, the PhC emitter has been shown to have an efficiency of 30% [91, 141] and is capable of withstanding temperatures up to 650 °C in argon [141].

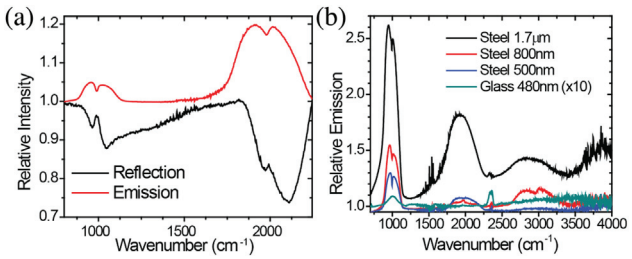

Figure 18 (a) Steel gratings generate a selective emission spectrum when heated to 200 °C. (b) Etch depth of the gratings can significantly impact the strength of the response, as shown by the emission of gratings varied from 500 nm to 1.7 μm deep. The use of a conductive metal such as steel is important, evidenced by the low relative emission of a similar structure fabricated using glass. Reproduced with permission [140]. Copyright 2010, OSA Publishing.

The other structure used in emitter design is the inverse opal, created using the self-assembling nature of microspheres to make an fcc lattice. The space between the spheres is then filled with the desired material and the spheres are dissolved, leaving spherical air holes behind [127]. Silica spheres are commonly used and removed via an HF etch [127, 142]. Polymer spheres have also been reported [181], but can only be used when the next process is relatively low temperature. The spheres are then coated via chemical vapor deposition (CVD) or atomic layer deposition (ALD) to create a scaffold made of silicon [127], carbon [181],or even the final metal [142]. The scaffold can then be coated in a refractory metal to further enhance or adjust the selectivity [142, 181]. A top-down method utilizing etching with modulated photocurrent can create an inverse opal-like structure in silicon. The pore size can further be tuned through oxidation and oxide removal cycles. This silicon scaffold can then be coated with a refractory metal as in previous methods [128].

Thermal stability is a major issue in 3D PhCs as the unique optical behavior is dependent on structure uniformity and small feature sizes. Grain formation in the metal layer can warp the structure [182]. Interactions such as eutectic formation or material pooling can ruin the metal coating and nanostructures [142]. The addition of protective layers can preserve the structure to higher temperatures. Use of a SiO_2 layer between Pt and Si can prevent eutectic formation [128]. Alumina and hafnia can improve both tungsten adhesion to the scaffold and overall stability at temperatures up to 1000 °C in forming gas, as seen in Fig. 21. However, as the temperature approaches 1400 °C, alumina-coated inverse opal PhCs lose their periodicity and become unusable [142].

3.2 Metamaterials In the past 2 decades, there has been a significant research focus on the development of metamaterials (MMs). In general, a metamaterial is an engineered material consisting of periodic patterns that are smaller than the wavelength of interest and can produce or behave with characteristics that are not found in nature. Using this definition, photonic crystals qualify as a subset of metamaterials. However, they are generally discussed separately as the PhC structure period is on the order of the size of the target wavelength, meaning interference and diffraction dominate the optical interactions. MM patterns are much smaller than the target wavelength, so more subtle

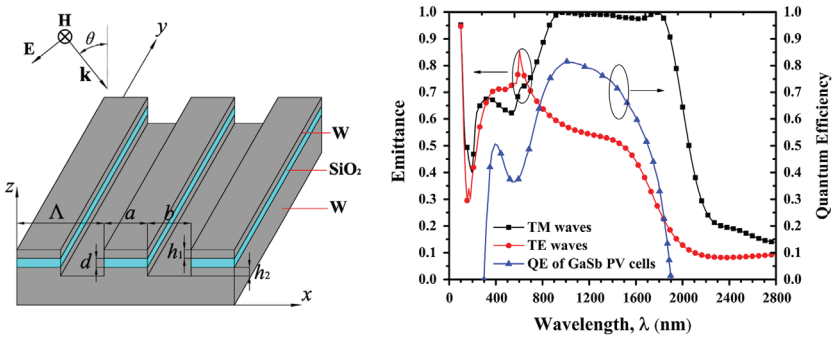

Figure 19 (Left) Cutout of a trilayer $W/SiO_2/W$ grating structure. (Right) Calculated emittance of TE and TM waves show a se-lective response. The quantum efficiency of a GaSb PV cell is overlaid for comparison. Adapted with permission [167]. Copyright 2015, Elsevier.

electromagnetic field interactions dominate. MMs are designed to exhibit particular permittivity and permeability coefficients, thus impacting the impedance, or refractive index, of the material [183]. Natural materials can either have a negative permittivity or a negative permeability, but never both at the same time. This means a natural refractive index is always positive and may contain an imaginary component. Recently, negative refractive indices have been realized using man-made structures [184] and have led to research advances in the development of invisibility cloaks [185], perfect lenses [186], and other custom dielectrics. The advanced manipulation of electromagnetic radiation with MMs has also led to the development of perfect absorbers and emitters, which have additional applications in photodetector [187, 188] and photovoltaic enhancement [189–191].

A standard metamaterial consists of a dielectric substrate with a subwavelength, periodic pattern made of a conducting material on top. They are usually fabricated using photo- or electron beam lithography, depending on the necessary resolution required for the pattern, on top of the dielectric substrate. Physical vapor deposition is used to lay down the metal on top of the resist pattern. A process called liftoff removes the extra metal so that only the area without resist remains metalized. The designs used for MMs are as varied as their many applications and creators. What they have in common is the induction of fields that interact with light in customized, novel ways.

3.2.1 Emission mechanism There are several design components that the makers of metamaterials use to manipulate the effective permittivity and permeability of a material. The most obvious variables are the geometry and layout of the design: for example, split-ring resonators (SRRs) are able to interact with impinging light based on the induction of current in the metallic periodic structure. If you wish to interact with the magnetic field using an SRR, as in Fig. 22a, the light should enter the pattern through the side, as shown by the wave vector, $\boldsymbol{k}$, rather than the top of the wafer [184]. The magnetic component of the wave travels perpendicular to the plane of the pattern and induces a current in the conductive metal. This current in turn produces a magnetic field that can either enhance or counteract the impinging magnetic component of the wave.

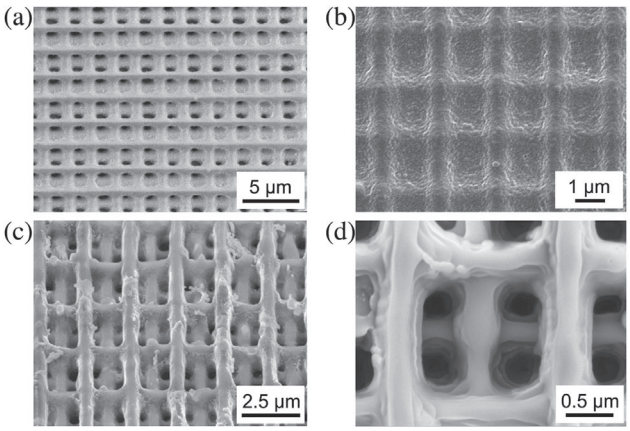

Figure 20 Eight-layer silica woodpiles consist of alternating layers of rods that are coated in a thin film of metal, such as 100 nm of (a) tungsten or (c) molybdenum. Overcoating can lead to almost complete infiltration of the sample, as shown with molybdenum (b). Higher magnification and acceleration voltages allow images of the silica rods within the molybdenum shell (d). Reproduced with permission [141]. Copyright 2008, American Chemical Society.

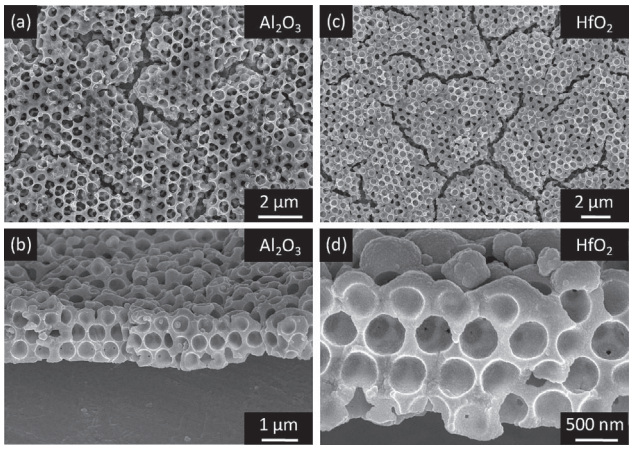

Figure 21 Top view and fracture cross section scanning electron micrographs of (a, b) alumina- and (c,d) hafnia-protected tungsten inverse opal PhCs perform equally well at 1000 °C. The samples were heated for 12 h in forming gas. Reproduced with permission [142]. Copyright 2011, American Chemical Society.

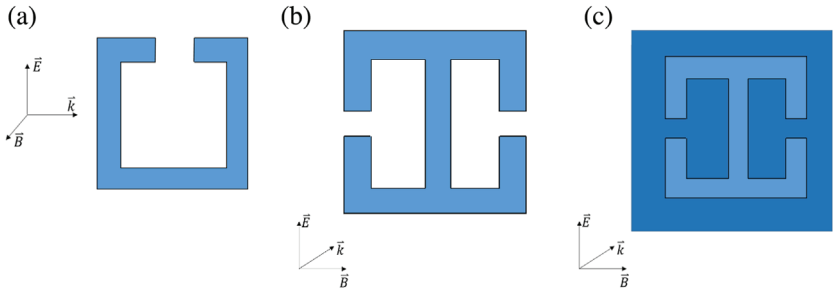

Figure 22 (a) A SRR interacts with the magnetic component of light, resulting in a change in effective permeability. (b) An ERR interacts with the electric component of light, changing the effective permittivity of the material. In both (a) and (b), the pattern is made of metal and is fabricated on a dielectric substrate. (c) Combining an ERR with a metallic back allows manipulation of the effective permittivity and permeability of a metamaterial. This structure consists of a metal thin film, a dielectric spacing layer, and finally the metal patterns.

As the pattern is smaller than the wavelength of the target frequency, the perceived effect is a uniform change in effective permeability. The electric component of light can also produce an induced magnetic field in the SRR, but this effect is much weaker than that produced by the magnetic component [192]. An electric ring resonator (ERR), seen in Fig. 22b, works in a similar fashion, but affects the permittivity of the material due to interactions with the electric wave component and the induced electric field.

Based on how each component of an electromagnetic wave interacts with the planar metal patterning of a MM, a structure that manipulates both components at the same time must exist in three dimensions. As seen in Fig. 22c, such a structure consists of an ERR on a dielectric substrate with a metallic grounding plane on the back. Some designs call for wires on the back rather than a full grounding plane [193], but the effect is essentially the same. The ERR affects the permittivity as described before, but the back plane also couples with the current to induce a magnetic field, affecting the permeability of the material. The orientation of the MM pattern relative to in the incident light, or the desired direction of emitted light, can drastically change what component of the electromagnetic wave is changed and must be taken into account in the design process.

3.2.2 Modeling and theory The gaps between metalized regions on a MM play an important role in determining the resonant frequency of the device. Two metal regions near to each other will induce a capacitance, further changing the induced fields present. Increasing or decreasing the distance between the metal regions will change this capacitance and its impact on the device resonant frequency. Adjustments in the resonator split gaps or the proximity of unit cells will change the effective plasma frequency, thereby changing the MM permittivity response [193]. Simulation data has shown that decreasing the gap enhances the field strength of a SRR [194, 195]. The resonant frequency also shifts as the gap width increases.

The layer thickness of the device also has an impact on the characteristics of a MM. Traditional electromagnetic wave absorbers have to have a thickness of $\lambda_o/4$ in order to be effective [196]. MM absorbers do not require this depth, with thicknesses as low as $\lambda_o/75$ being reported [196], but layer thickness does have to be taken into account during the design process. Calculations using the Drude–Lorentz model show that for very small thicknesses, the absorptivity goes to zero [196]. Based on the parameters for the dielectric and metal materials in use, an optimum thickness is reached where the absorptivity gets as close to unity as is possible. As the material thickness is increased beyond this point, the frequency bandwidth increases [196].

To operate as a perfect absorber, a material needs to have little to no transmission and reflection of impinging light. Minimizing reflection occurs when the impedance of the material is matched to the impedance of free-space. Optical impedance can be calculated from the material's reflectance and transmission coefficients, found either through simulation or experimentally [197]. The transmission through a unit cell of the design must also be minimized such that $T(\omega) \rightarrow 0$ as more layers are added. Once these criteria have been met, the absorbance of the material maximizes at the resonant frequency [197]. Theoretically, absorbance can reach 100% at this frequency. In practice, slight irregularities in the pattern from the fabrication process or material constraints depending on the frequency of interest can make the actual absorbance percentage smaller.

These relationships make it possible to calculate the complex optical constants of a given MM design [193] in a simulation environment such as finite-difference time domain solver Microwave Studio® produced by CST (Computer Simulation Technology). The design can then be manipulated within the simulation to change the effective permittivity and permeability to the desired values before fabrication. Slight variances to FDTD include the finite integration technique (FIT), where the integral forms of Maxwell's equations are used rather than the differential form. This form of the equations uses fewer resources and allows for faster simulations [117]. Using this method in the transient mode results in implementation that is nearly identical to the FDTD method.

Circuit models have also been applied to metamaterial designs. Use of an LC model is sufficient to calculate the resonant frequency of disks, squares, crosses, and strips [198]. Expansion to an RLC model allows calculation of the FWHM and Q-factor in addition to the resonant frequency [199]. In both models, capacitance (C_m) comes from the dielectric spacer that separates the metallic ground

plane from the patterned layer. Kinetic inductance (L_k) and magnetic inductance (L_m) come from the magnetic energy stored in the dielectric spacer and the kinetic energy of the electrons in the metal, respectively. The additional resistances (R_1 and R_2) come from the sheet resistance of the metal used in the top and bottom layers [200]. These quantities can be used to directly calculate resonant frequency (Eq. (1)), FWHM (Eq. (2)), and Q-factor (Eq. (3)) of the design using the equations below [199]. The results match traditional FDTD simulation well enough to be used for inital design parameter determination.

$$f_r = \frac{1}{2\pi}\sqrt{\frac{2}{C_m(2L_m + L_{k1} + L_{k2})}}, \quad (1)$$

$$\Delta f = \frac{1}{2\pi}\left(\frac{R_1 + R_2}{2L_m + L_{k1} + L_{k2}}\right), \quad (2)$$

$$Q = \frac{2}{R_1 + R_2}\sqrt{\frac{2L_m + L_{k1} + L_{k2}}{2C_m}}. \quad (3)$$

3.2.3 Structures Several different design schemes have become popular for the fabrication of metamaterial selective emitters. Depending on the wavelength in question, their size and fabrication method also varies. As the wavelength of interest gets shorter, into the near infrared or visible range, the MM pattern must also scale smaller, requiring fabrication methods with greater resolution such as electron beam or focused ion beam (FIB) [196]. These serial processing methods are slow and costly compared to flood methods like photolithography, so research into general MM characteristics typically focuses on the long wavelength microwave regime.

One common pattern is the repeated cross, as shown in Fig. 23. The resonant frequency of the cross is proportional to its length, so this pattern can easily be scaled to interact with different wavelengths. The back grounding plane is thick enough that light cannot transmit through it, ensuring a high absorption rate [201, 202]. Crosses of different sizes can be combined in a single unit cell to create a spectrum with multiple peaks. To prove a pattern's ability to emit the spectrum that it absorbs, experimental absorption and emission data was taken for the single and dual band systems. Figure 24a shows a close match with near unity absorption and emission at the resonant frequency for the single band pattern. The dual band pattern clearly responds with similar absorption and emission profiles for the two resonant frequencies (Fig. 24b), though their response is not quite at 100% at the peak [202].

Metamaterial samples are often made of gold, aluminum, or copper with a dielectric as the spacer, such as alumina. The desire to use these samples in high temperature applications has led to the use of a tungsten and other refractory metals as the conductor [9, 191, 203–206] and exploration of alternate dielectrics such as spin-on glass [207], aluminum nitride [203, 208], strontium titanate [209], or $Ge_2Sb_1Te_4$ [210]. Metamaterials were first used as perfect absorbers in 2008, when Landy et al. fabricated and analyzed an ERR and wire pattern sized to correspond to a peak wavelength in the microwave

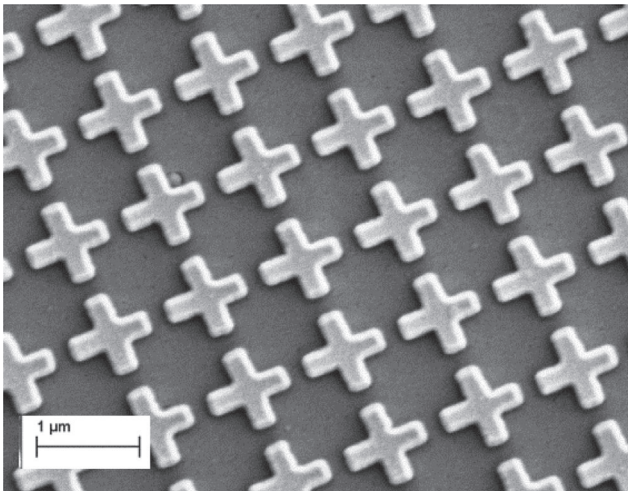

Figure 23 Cross patterns are commonly used in mid-IR MM applications. Shown is a SEM image of a platinum and alumina MM designed to emit at 3.7 μm [201].

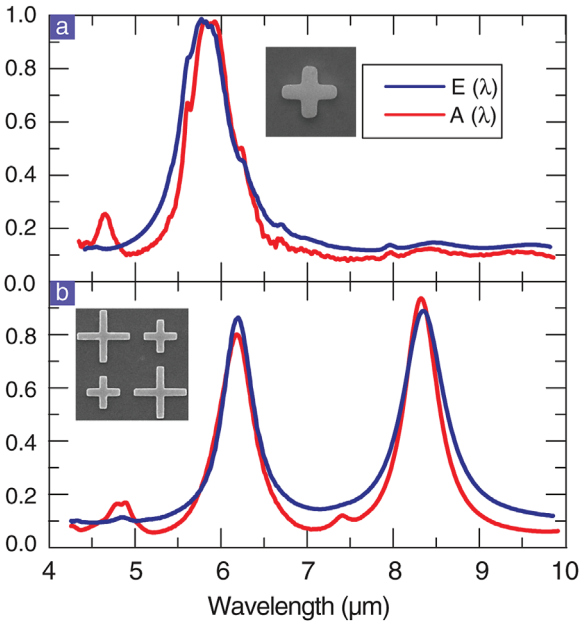

Figure 24 (a) Comparison of experimental absorptivity (red) and emissivity (blue) show good agreement for a single cross metamaterial design. (b) Similar agreement is found for the dual-band response that comes from a pattern incorporating two different sized crosses. Adapted with permission [202]. Copyright 2011, American Physical Society.

regime [193]. The experimental absorption achieved an 88% absorption rate at the peak frequency of 11.48 GHz, compared to the simulated peak of 96% at the same frequency. The sample absorption was highly dependent on the angle of incidence, with a steep absorbance drop-off after 5°. The absorbance after 16° was simulated to be less than 0.5. Once the concept was proven feasible, the process of scaling down the MM structures to work with smaller wavelengths began. What began in the microwave regime [211] soon worked its way through the far-infrared [212], mid-IR [202], near-IR [191], and even slightly into the visible [213]. At this point, the physical limitations of present fabrication techniques halted further shifts up the frequency range. As seen in Fig. 25, the features required for NIR wavelengths compared to those for far IR are much less complex due fabrication limits.

Much like how the 3D orientation of the MM affects whether it interacts with the electric or magnetic component of a photon, rotating the material about its center can change its interaction with s- or p-polarized light [215]. This knowledge can be used to selectively filter light of a given polarization [216], but generally similar performance for all polarization orientations is desired for efficient absorbers. Creating a polarization-independent absorber can be accomplished by increasing the number of symmetry axes of the pattern. If the sample will be aligned with one polarization direction but the capture of both is desired, four-axis symmetry is required [196]. The 90° symmetry angle means that no matter which pattern arm is parallel with the electric field, the correct electron motion and capacitive effect will be induced. Patterns as simple as rectangular bars [217] or squares [218] can achieve this level of polarization independence, as can other designs with four axis of symmetry like crosses [196]. However, avoiding symmetry in dual-band designs can sometimes be beneficial, as it is possible to get strong peaks at different wavelengths when the material is exposed to two different polarizations [200].

Increasing the acceptable polarization angles requires increasing the number of axis of symmetry. This can be done literally by implementing a snowflake-like pattern, also known as a dendritic resonator [219], with several symmetrical arms. Simulations of this pattern show near unity absorption despite rotating the incident polarization any angle between 0 and 90° [219]. Polarization-insensitivity can also be accomplished by utilizing rotational symmetry in the pattern design. Metamaterial absorbers have been created using circles [220] or circular components like outer rings [221] that perform well at all polarization angles.

Metamaterial absorbers' ability to absorb light has been shown to be highly dependent on the angle of incidence. With typical ERRs, optimum absorption occurs when the light is normal to the absorber surface, with a sharp decrease in absorption when the incident angle becomes greater than 5° off normal [193]. As the incident angle increases, the parallel magnetic field strength decreases, reducing the ability to produce antiparallel currents in the two metallic layers of the metamaterial [196]. This drops the overall magnetic flux and, if the incident angle is wide enough, can prevent the resonant behavior that drives absorption. However, work has been done to create metamaterial patterns that can operate at wider angle ranges [212, 219, 221–223].

As with the polarization independent patterns, increasing the axes of symmetry creates a more robust pattern, allowing the absorption of less than ideally incident light. The snowflake-shaped pattern mentioned previously for its polarization-insensitivity maintains greater than 95% absorption for TE and TM polarized light incident at angles of up to 50° [219, 224]. Near unity absorption has been achieved for many different patterns, such as electric LC resonators [221] and crosses [222] at incident angles of up to 50° [221–223]. Absorption above 85% can be achieved at 60° incident angle for these designs, but then it dramatically drops off as the angle increases further, depending on the polarization. For some configurations, absorption can remain high up to 80° incidence for a single polarization [212].

Combining patterns of various sizes to create a custom absorption spectrum has been explored as well. One way to accomplish this is to create a complex repeated pattern that incorporates patterns of different sizes [202]. This induces resonance at multiple frequencies, creating a multi-band spectrum; for example, Zhang et al. [225] created a repeating pattern of different sized squares made of gold on a spacer layer of magnesium fluoride. The multiplexed squares, with sides length 0.95 and 1.35 μm, produced resonant responses at wavelengths of 3.67 and 5.01 μm, respectively [225]. Adding

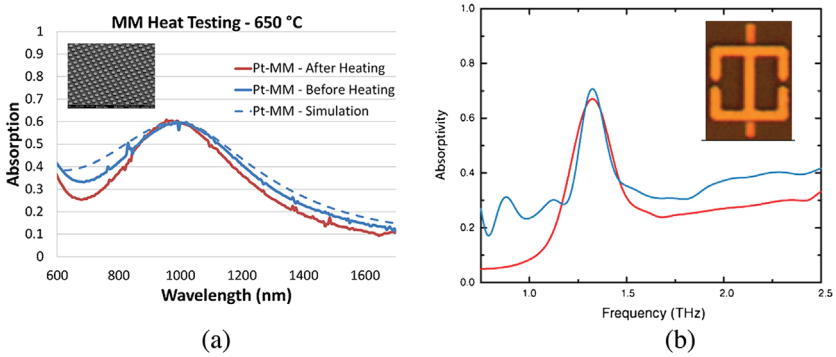

(a) (b)

Figure 25 (a) Simulated and experimental absorption of metamaterials designed for NIR. Inset is a scanning electron micrograph of the MM features, including several unit cells. Adapted with permission [191]. Copyright 2014, AIP Publishing. (b) Simulated and experimental absorption of metamaterials designed for far IR. Inset is a photograph of the fabricated unit cell. Adapted with permission [214]. Copyright 2008, OSA Publishing.

an even smaller set of squares to this pattern creates a tri-band spectral response. A similar technique has been performed using cross patterns to the same effect [202].

Another way to create this multiband effect is to create a single pattern with several split gaps and conducting wire lengths to again induce resonances at different frequencies. This method creates a more robust metamaterial, as multiple axes of symmetry are easier to incorporate rather than complicating the multiplexing scheme. An example of this is the cross-circular-loop resonator (CCLR), where the resonant behavior is determined by the position of the shorted stubs between the inner and outer ring. By moving the stubs closer together, the dual-band mode is activated. The dual-band response has been successfully created using multiple rings [226], split ring resonators [227], crosses [228], cross-hatches [229], and asymmetrical electric-field-coupled resonators [230].

To operate as an emitter, perfect absorbers must be heated. The addition of energy through the application of heat induces current flow in the metallic MM patterns. When enough thermal energy is added, photons will be emitted following the designed emission spectrum. The number of emitted photons at a given wavelength is a function of the designed emissivity at the wavelength times the blackbody emission curve at the emitter's operating temperature.

MM emitters designed for TPV applications were first reported in 2011 with the NIR cross pattern mentioned previously and shown in Fig. 24 [202]. To prove a pattern's ability to emit the spectrum that it absorbs, emission from the single- and dual-band systems was measured at several temperatures. As seen in Fig. 26, the emittance for each peak scaled along with temperature, roughly matching the corresponding blackbody output for that temperature. Conversion back to emissivity shows consistency regardless of measurement temperature.

Multiple emitters, originally designed and tested as perfect absorbers, were fabricated out of gold and a layer of benzocyclobutene. The emittance of a single peak and dual-band system was measured at temperatures between 100 and 300 °C. The spectral emittance measured for each device was proportional to the blackbody curve of the operating temperature. Across all temperatures, the emissivity of the metamaterial was approximately the same, measuring near unity at 6 μm for the single band sample and near 90% at about 6 and 8 μm for the dual-band sample [202]. Direct comparison between the measured absorptivity and normalized emissivity show good agreement, confirming the metamaterial behavior adheres to Kirchhoff's law.

Much like the polarization dependent absorbers described earlier, metamaterials can be designed to emit with a specific polarization. Linear and circular polarized light has been measured, making use of 3D metamaterial structures [233] and non-symmetrical 2D structures [231]. Both of these methods utilize the Stokes parameters to define and then optimize the polarization of emitted light through simulation. The 3D metamaterial utilized a wire grid array and a meanderline pattern separated by silica aerogel. This combination resulted in experimental measurements of 28% circularly polarized light and 77% linearly polarized light, with an average deviation of 5% for both polarizations [233]. The non-symmetrical 2D structures were generated via a genetic algorithm optimization technique [234]. This technique encodes the metamaterial design parameters such as unit cell size and thickness into 8-bit numbers and then the pattern geometry into binary 1s, metal, and 0s, air. Candidate patterns are combined and tested for fitness against the desired response. The highest performing patterns are combined and then tested again, continuing until the performance converges close to the desired polarization. Simulations showed circular polarization of 83.6% of the possible maximum, with emittance of 56%, as seen in Fig. 27. The same technique generated patterns producing elliptical polarization with emittance of

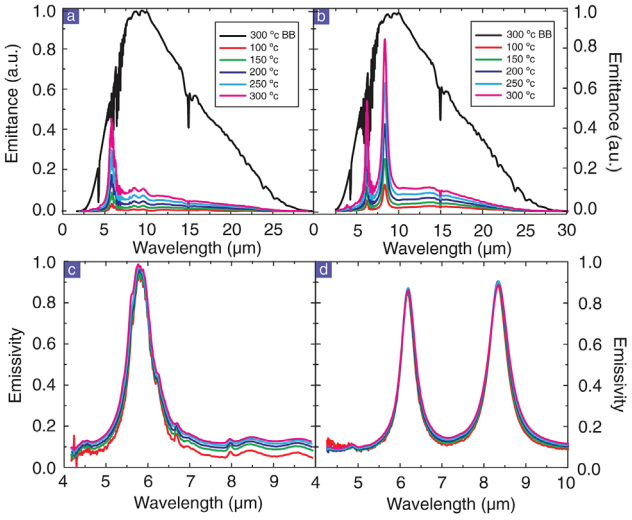

Figure 26 Measured emittance for a (a) single-band and (b) dual-band emitter at several temperatures shows output increases with increased temperature as would be expected. Calculation of emissivity for the (c) single-band and (d) dual-band emitters shows consistency across all measured temperatures. Reproduced with permission [202]. Copyright 2011, American Physical Society.

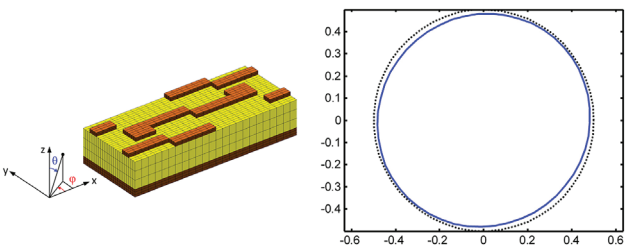

Figure 27 Use of the genetic algorithm optimization technique to generate the metamaterial unit cell on the left. A calculation of the resulting polarization shows almost complete circular polarization. Adapted with permission [231]. Copyright 2013, OSA Publishing.

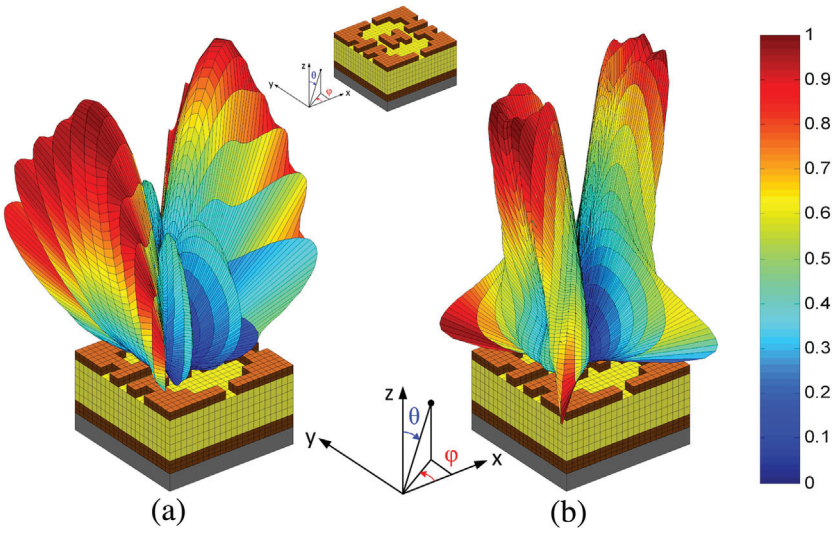

Figure 28 Genetic algorithm optimized MM unit cells (inset) are capable of controlling the angle at which emissivity peaks appear. These "butterfly-wing" emission patterns peak at 40° off normal and vary slightly for (a) TE and (b) TM waves. Adapted with permission [232]. Copyright 2013, OSA Publishing.

32%, and linear polarization with emittance of 21% at the desired wavelength [231].

As a corollary to the incident angle dependence, emission intensity can also be designed as a function of angle. Using the genetic algorithm optimization technique, complex patterns with four- and eightfold symmetry were simulated that have characteristic emission profiles at a single wavelength [232]. Both designs had peak emissivity at a 40° off-normal rather than at 0°, which is more common with metamaterials. The eightfold symmetry pattern created conical, azimuthally stable peak emission pattern, while the fourfold symmetry pattern created a "butterfly-wing" shape pattern, shown in Fig. 28, with peak emission symmetry only along one plane [232].

Most recently, research has turned toward more interesting materials and designs. Use of exotic dielectrics has led to the development of frequency tunable metamaterials whose peaks can be shifted by applying heat [209] or by choosing a different crystalline form of the dielectric [210]. Metallic nanowires have been incorporated into larger dielectric structures to create polarization independent emitters [204, 235]. Tungsten nanospheres coated in SiO_2 and an additional layer of tungsten generates an emission curve similar to that of a 2D PhC [205]. Concave grating metamaterials generate several sharp peaks due to the multiple polariton modes that appear [235]. Broadband peaks can be produced using a thermally robust material through SiC antenna meta-surfaces, a 3D structure, on silicon [236]. These structures bring to light additional points for customization, allowing flexibility in the design process.

Though much progress is being made on the design and optical behavior of metamaterial emitters, little testing has been done on their high temperature performance. At the time of this writing, the highest published emittance temperature for gold is 300 °C [192] and for aluminum is 400 °C [220]. Recent work by Shemelya et al. has measured selective emittance at up to 615 °C utilizing platinum as the conducting metal [191]. Further research of these patterns has looked at performance when changing dielectrics and using capping layers [201] and other groups have looked to even higher temperature cycling [206]. Introduction of a thin dielectric capping layer resulted in a slight red shift of the peak in the NIR, though this effect was less apparent as the pattern size increased [201]. Heat testing has shown stability of the nanostructures as high as 1300 K in a purely argon atmosphere [206] and 750 °C, or 1023 K, in air [9]. SEM images of the Pt NIR features before and after heating at 750 °C can be seen in Fig. 29.

4 Conclusions Increasing the efficiency of thermophotovoltaic systems requires an efficient selective emitter that radiates the majority of its energy near the band gap of the TPV diode. Early research in this area provided plasma and rare earth element-based emitters while more recent

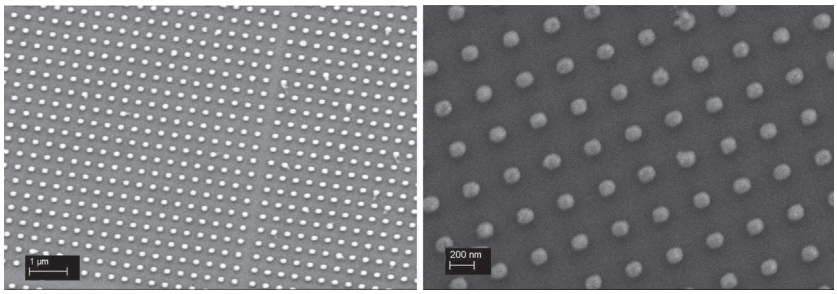

Figure 29 Heating of a platinum on silicon nitride metamaterial emitter with features at 180 nm show little to no degradation of the metallic pattern. SEM images of before (left) and after (right) heating in atmosphere [201].

efforts have focused on nanostructured photonic crystals and metamaterials. Although each approach exhibits good selective behavior, they also have their drawbacks. Plasma and rare earth sources can withstand high temperatures with little to no degradation, but the spectra they produce are linked to their atomic makeup and cannot be changed. Therefore, the TPV diode must be designed around the emission spectrum or an inefficient match must be made. Conversely, photonic crystals and metamaterials provide engineerable spectra that can be designed to match a given TPV diode, but present designs cannot handle high temperatures. Most testing in an oxygenated atmosphere to date has been below 500 °C, with the higher 1300 K temperatures occurring in an inert atmosphere such as argon or a vacuum. Although the vacuum results would translate well to space applications, it would be difficult to maintain in a terrestrial device. The conducting materials used in these applications typically melt or degrade at very high temperatures. Recent work with new materials such as steel and platinum can reduce this issue, making nanostructures the selective emitter of choice even for high temperature applications.

Though several kinds of selective thermal emitters are available, metamaterials offer the most potential in terms of wavelength tunability and application customization. Though present research utilizes many low-temperature devices, platinum has been shown to be a promising candidate for high temperature applications. Further research into this material and other refractory metals may yet produce a thermally stable emitter for direct integration into terrestrial devices.

Acknowledgements This material is based upon work supported by the National Science Foundation Grant No. ECCS-1055203, National Science Foundation Graduate Research Fellowship under Grant No. DGE-1000169618, the Air Force Office of Scientific Research Grant No. FA9550-11-10061. The authors would like to thank Dr. Corey Shemelya for discussions about photonic crystals.

References

[1] R. E. Nelson, Semicond. Sci. Technol. **18**, S141–S143 (2003).
[2] D. F. DeMeo, A. S. Licht, T. E. Vandervelde, C. M. Shemelya, and C. M. Downs, Thermophotovoltaics: An Alternative to and Potential Partner with Rectenna Energy Harvesters. in: Rectenna Solar Cells, edited by I. G. Moddel and S. Grover, Part IV (Springer-Verlag, New York, Inc., 2013), pp. 371–390.
[3] D. Chubb, Fundamentals of Thermophotovoltaic Energy Conversion (Elsevier, Oxford, 2007).
[4] N.-P. Harder and P. Wurfel, Semicond. Sci. Technol. **18**, S151–S157 (2003).
[5] H. Kolm, Solar-Battery Power Source, Quarterly Progress Report, Solid State Research, Group 35 (MIT Lincoln Laboratory, Lexington, MA, 1956), p. 13.
[6] G. Guazzoni, Appl. Spectroscopy **26**, 14–17 (1972).
[7] J. J. Werth, Thermo-photovoltaic converter with radiant energy reflective means, U.S. Patent 3,331,707 (1963).
[8] G. Guazzoni, AIP Conf. Proc. **738**, 3–12 (2004).
[9] N. Pfiester, N. Naka, and T. Vandervelde, in: Proc. 31st Eur. PV Solar Energ Conf. and Exhibition (Hamburg, Germany, 2015), pp. 55–58.
[10] B. Wernsman, R. R. Siergiej, S. D. Link, R. G. Mahorter, M. N. Palmisiano, R. J. Wehrer, R. W. Schultz, G. P. Schmuck, R. L. Messham, S. Murray, C. S. Murray, F. Newman, D. Taylor, D. M. DePoy, and T. Rahmlow, IEEE Trans. Electron Devices **51**, 512–515 (2004).
[11] V. Rinnerbauer, S. Ndao, Y. X. Yeng, W. R. Chan, J. Senkevich, J. D. Joannopoulos, M. Soljacic, and I. Celanovic, Energy Environ. Sci. **5**, 8815 (2012).
[12] A. W. Bett and O. V. Sulima, Semicond. Sci. Technol. **18**, S184–S190 (2003).
[13] M. G. Mauk and V. M. Andreev, Semicond. Sci. Technol. **18**, S191–S201 (2003).
[14] T. Schlegl, F. Dimroth, A. Ohm, and A. W. Bett, Seventh World Conference on Thermophotovoltaic Generation of Electricity 285–293 (AIP, Madrid, 2004).
[15] D. F. DeMeo and T. E. Vandervelde, MRS Proc. **1329**, 119–124 (2011).
[16] D. DeMeo, C. Shemelya, C. Downs, S. Magden, A. Licht, T. E. Vandervelde, C. Dhital, S. Wilson, T. Rotter, and G. Balakrishnan, J. Electron. Mater. **43**, 902–908 (2014).
[17] M. W. Dashiell, J. F. Beausang, H. Ehsani, G. J. Nichols, D. M. Depoy, L. R. Danielson, P. Talamo, K. D. Rahner, E. J. Brown, S. R. Burger, P. M. Fourspring, W. F. Topper Jr., P. F. Baldasaro, C. A. Wang, R. K. Huang, M. K. Connors, G. W. Turner, Z. A. Shellenbarger, G. Taylor, J. Li, R. Martinelli, D. Donetski, S. Anikeev, G. L. Belenky, and S. Luryi, IEEE Trans. Electron Devices **53**, 2879–2891 (2006).
[18] M. Tan, L. Ji, Y. Wu, P. Dai, Q. Wang, K. Li, T. Yu, Y. Yu, S. Lu, and H. Yang, Appl. Phys. Express **7**, 96601 (2014).
[19] W. Li, J. Lammasniemi, A. Kazantsev, R. Jaakola, T. Makela, and M. Pessa, Electron. Lett. **34**, 406–407 (1998).
[20] V. M. Andreev, V. P. Khvostikov, V. D. Rumyantsev, S. V. Sorokina, and M. Z. Shvarts, in: Conference Record of 28th IEEE Photovoltaic Specialists Conference – 2000 (Cat. No. 00CH37036) 1265–1268 (IEEE). DOI:10.1109/PVSC.2000.916120.
[21] Y. Wang, Sol. Energy Mater. Sol. Cells **141**, 391–397 (2015).
[22] V. M. Aroutiounian, G. S. Shmavonyan, O. A. Zadoyan, K. M. Gambaryan, and A. M. Zadoyan, J. Contemp. Phys. **49**, 258–263 (2014).
[23] L. D. Woolf, Sol. Cells **19**, 19–38 (1986).
[24] A. Datas, Sol. Energy Mater. Sol. Cells **134**, 275–290 (2015).
[25] D. Wilt, R. Wehrer, M. Palmisiano, M. Wanlass, and C. Murray, Semicond. Sci. Technol. **18**, S209–S215 (2003).
[26] D. M. Wilt, N. S. Fatemi, P. P. Jenkins, R. W. Hoffman, G. A. Landis, and R. K. Jain, in: Conference Record 25th IEEE Photovoltaic Specialists Conference – 1996 (IEEE, 1996), pp. 43–48. DOI:10.1109/PVSC.1996.563942.
[27] S. Wang, IEEE J. Quantum Electron. **10**, 413–427 (1974).
[28] M. Kimura, K. Okahara, and T. Miyamoto, J. Appl. Phys. **50**, 1222 (1979).
[29] T. Coutts, J. Renew. Sustain. Energy Rev. **3**, 77–184 (1999).
[30] R. J. Dziendziel, P. F. Baldasaro, and D. M. DePoy, Tandem filters using frequency selective surfaces for enhanced conversion efficiency in a thermophotovoltaic energy

conversion system. U.S. Patent 7166797 B1, issued Jan. 23, 2007.
[31] T. Bauer, Thermophotovoltaics (Springer, Berlin, Heidelberg, 2011), DOI:10.1007/978-3-642-19965-3.
[32] G. W. Charache, J. L. Egley, D. M. Depoy, L. R. Danielson, M. J. Freeman, R. J. Dziendziel, J. F. Moynihan, P. F. Baldasaro, B. C. Campbell, C. A. Wang, H. K. Choi, G. W. Turner, S. J. Wojtczuk, P. Colter, P. Sharps, M. Timmons, R. E. Fahey, and K. Zhang, J. Electron. Mater. **27**, 1038–1042 (1998).
[33] L. M. Fraas, J. E. Avery, H. X. Huang, and R. U. Martinelli, Semicond. Sci. Technol. **18**, S165–S173 (2003).
[34] T. D. Rahmlow, D. M. DePoy, P. M. Fourspring, H. Ehsani, J. E. Lazo-Wasem, and E. J. Gratrix, AIP Conf. Proc. **890**, 59–67 (2007).
[35] R. T. Kristensen, J. Appl. Phys. **95**, 4845 (2004).
[36] C. M. Shemelya, D. F. DeMeo, and T. E. Vandervelde, Appl. Phys. Lett. **104**, 21115 (2014).
[37] J. E. Raynolds, B. A. Munk, J. B. Pryor, and R. J. Marhefka, J. Appl. Phys. **93**, 5346 (2003).
[38] J. G. Mutitu, S. Shi, A. Barnett, and D. W. Prather, Energies **3**, 1914–1933 (2010).
[39] T. J. Coutts and M. C. Fitzgerald, Sci. Am. **279**, 90–95 (1998).
[40] S. Jin, M. Lim, S. S. Lee, and B. J. Lee, Opt. Express **24**, A635 (2016).
[41] S. J. Petersen, S. Basu, and M. Francoeur, Photonics Nanostructures – Fundam. Appl. **11**, 167–181 (2013).
[42] A. Karalis and J. D. Joannopoulos, Nat. Publ. Group. Sci. Rep. **6**, 28472 (2016).
[43] S.-A. Biehs, M. Tschikin, R. Messina, and P. Ben-Abdallah, Appl. Phys. Lett. **102**, 131106 (2013).
[44] M. Planck, The Theory of Heat Radiation (P. Blakiston's Son and Co., Philadelphia, 1914).
[45] T. S. Kuhn, Black-Body Theory and the Quantum Discontinuity (The University of Chicago Press, Chicago, 1978), pp. 1894–1912.
[46] G. R. Kirchhoff, Investigations on the Solar Spectrum and the Spectra of the Chemical Elements, 2nd ed. (Ferd. Dummler's Publishing House, Berlin, 1862), pp. 571–598.
[47] A. Fridman, Plasma Chemistry (Cambridge University Press, Cambridge, 2008), pp. 12–91.
[48] W. A. Ranken, G. M. Grover, and E. W. Salmi, J. Appl. Phys. **31**, 2140 (1960).
[49] J. Jonkers and J. A. M. Van Der Mullen, J. Quantum Spectrosc. Radiat. Transf. **61**, 703–709 (1999).
[50] F. G. Baksht and V. F. Lapshin, Tech. Phys. Lett. **23**, 961–963 (1997).
[51] R. Lowe, C. Goradia, M. Goradia, and D. L. Chubb, J. Appl. Phys. **68**, 5033 (1990).
[52] N. Y. Orlov and V. E. Fortov, Dokl. Phys. **370**, 34–37 (2000).
[53] M. Rosenberg and R. D. Smirnov, IEEE Trans. Plasma Sci. **38**, 1–9 (2010).
[54] K. H. Becker, K. H. Schoenbach, and J. G. Eden, J. Phys. D. Appl. Phys. **39**, R55–R70 (2006).
[55] J. Xue and J. A. Hopwood, IEEE Trans. Plasma Sci. **35**, 1574–1579 (2007).
[56] P. W. Selwood, J. Am. Chem. Soc. **52**, 4308–4316 (1930).
[57] P. Wijrfel and W. Ruppel, Sol. Cells **10**, 257–271 (1983).
[58] J. C. G. Bünzli, S. Comby, A. S. Chauvin, and C. D. B. Vandevyver, J. Rare Earths **25**, 257–274 (2007).
[59] F. Wang and X. Liu, Chem. Soc. Rev. **38**, 976 (2009).
[60] J. Lucas, P. Lucas, T. Le Mercier, A. Rollat, and W. Davenport, Rare Earths: Science, Technology, Production, and Use (Elsevier B.V., Amsterdam, 2015), DOI:10.1016/B978-0-444-62735-3.00008-5.
[61] A. Licciulli, D. Diso, G. Torsello, S. Tundo, A. Maffezzoli, M. Lomascolo, and M. Mazzer, Semicond. Sci. Technol. **18**, S174–S183 (2003).
[62] A. Freeman and R. Watson, Phys. Rev. **127**, 2058–2075 (1962).
[63] V. V. Golovlev, C. H. Winston Chen, and W. R. Garrett, Appl. Phys. Lett. **69**, 280 (1996).
[64] G. Torsello, M. Lomascolo, A. Licciulli, D. Diso, S. Tundo, and M. Mazzer, Nature Mater. **3**, 632–637 (2004).
[65] R. S. Roth and S. J. Schneider, Part I. J. Res. Natl. Bur. Stand. A **64A**, 309 (1960).
[66] G. Adachi and N. Imanaka, Chem. Rev. **98**, 1479–1514 (1998).
[67] D. Diso, A. Licciulli, A. Bianco, M. Lomascolo, G. Leo, M. Mazzer, S. Tundo, G. Torsello, and A. Maffezzoli, Mater. Sci. Eng. B **98**, 144–149 (2003).
[68] A. Licciulli, A. Maffezzoli, D. Diso, S. Tundo, M. Rella, G. Torsello, and M. Mazzer, J. Sol-Gel Sci. Technol. **26**, 1119–1123 (2003).
[69] N. Nakagawa, H. Ohtsubo, Y. Waku, and H. Yugami, J. Eur. Ceram. Soc. **25**, 1285–1291 (2005).
[70] B. Bitnar, W. Durisch, J. C. Mayor, H. Sigg, and H. R. Tschudi, Sol. Energy Mater. Sol. Cells **73**, 221–234 (2002).
[71] H. Wang, H. Ye, and Y. Zhang, Sci. China Technol. Sci. **57**, 332–338 (2014).
[72] D. L. Chubb and R. A. Lowe, J. Appl. Phys. **74**, 5687–5698 (1993).
[73] M. G. Krishna, R. G. Biswas, and A. K. Bhattacharya, J. Phys. D: Appl. Phys. **30**, 1167–1174 (1997).
[74] R. A. Lowe, D. L. Chubb, S. C. Farmer, and B. S. Good, Appl. Phys. Lett. **64**, 3551–3553 (1994).
[75] V. Tomer, R. Teye-Mensah, J. C. Tokash, N. Stojilovic, W. Kataphinan, E. A. Evans, G. G. Chase, R. D. Ramsier, D. J. Smith, and D. H. Reneker, Sol. Energy Mater. Sol. Cells **85**, 477–488 (2005).
[76] R. Teye-Mensah, V. Tomer, W. Kataphinan, J. C. Tokash, N. Stojilovic, G. G. Chase, E. A. Evans, R. D. Ramsier, D. J. Smith, and D. H. Reneker, J. Phys.: Condens. Matter. **16**, 7557–7564 (2004).
[77] A. Licciulli, A. Maffezzoli, D. Diso, S. Tundo, M. Rella, G. Torsello, and M. Mazzer, J. Sol-Gel Sci. Technol. **32**, 247–251 (2004).
[78] W. J. Tobler and W. Durisch, Appl. Energy **85**, 371–383 (2008).
[79] W. J. Tobler and W. Durisch, in: 7th Conference on Thermophotovoltaic Generation of Electricity (2007), pp. 37–47.
[80] M. Ghanashyam Krishna, M. Rajendran, D. R. Pyke, and A. K. Bhattacharya, Sol. Energy Mater. Sol. Cells **59**, 337–348 (1999).
[81] L. G. Ferguson and F. Dogan, Mater. Sci. Eng. B **83**, 35–41 (2001).
[82] L. G. Ferguson and F. Dogan, J. Mater. Sci. **37**, 1301–1308 (2002).
[83] S. I. Serdyukova and B. N. Zakhariev, Phys. Rev. A **46**, 58–63 (1992).

[84] T. F. Boggess, L. Zhang, D. G. Deppe, D. L. Huffaker, and C. Cao, Appl. Phys. Lett. **78**, 276 (2001).
[85] C. M. Shemelya and T. E. Vandervelde, J. Electron. Mater. **41**, 928–934 (2012).
[86] C. M. Shemelya and T. E. Vandervelde, MRS Proc. **1208**, 127–132 (2009), DOI: 1208-O16-06.
[87] J. D. Joannopolous, S. G. Johnson, J. N. Winn, and R. D. Meade Photonic Crystal: Molding the Flow of Light (Princeton University Press, Princeton, 2011).
[88] E. Yablonovitch, Phys. Rev. Lett. **58**, 2059–2062 (1987).
[89] S. John, Phys. Rev. Lett. **58**, 2486–2489 (1987).
[90] M. U. Pralle, N. Moelders, M. P. McNeal, I. Puscasu, A. C. Greenwald, J. T. Daly, E. A. Johnson, T. George, D. S. Choi, I. El-Kady, and R. Biswas, Appl. Phys. Lett. **81**, 4685–4687 (2002).
[91] S. Y. Lin, J. Moreno, and J. G. Fleming, Appl. Phys. Lett. **83**, 380 (2003).
[92] N. Jovanović, I. Čelanović, and J. Kassakian, AIP Conf. Proc. **890**, 47–55 (AIP, 2007).
[93] W. M. Robertson and M. S. May, Appl. Phys. Lett. **74**, 1800 (1999).
[94] L. Martín-Moreno, F. García-Vidal, H. Lezec, K. Pellerin, T. Thio, J. Pendry, and T. Ebbesen, Phys. Rev. Lett. **86**, 1114–1117 (2001).
[95] B. J. Lee, C. J. Fu, and Z. M. Zhang, Appl. Phys. Lett. **87**, 71904 (2005).
[96] H. Y. Ryu and M. Notomi, Opt. Lett. **28**, 2390 (2003).
[97] I. Celanovic, D. Perreault, and J. Kassakian, Phys. Rev. B **72**, 2–7 (2005).
[98] Y.-B. B. Chen and Z. M. M. Zhang, Opt. Commun. **269**, 411–417 (2007).
[99] Z. M. Zhang and L. P. Wang, Int. J. Thermophys. **34**, 2209–2242 (2013).
[100] A. Richel, N. P. Johnson, and D. W. McComb, Appl. Phys. Lett. **76**, 1816 (2000).
[101] C. M. Cornelius and J. P. Dowling, Phys. Rev. A **59**, 4736–4746 (1999).
[102] S.-Y. Lin, J. G. Fleming, E. Chow, J. Bur, K. K. Choi, and A. Goldberg, Phys. Rev. B **62**, R2243–R2246 (2000).
[103] A. Moroz, Europhys. Lett. **46**, 419–424 (1999).
[104] S. G. Babiker, M. O. Sid-ahmed, and S. Yong, Int. J. Energy, Inf. Commun. **5**, 1–16 (2014).
[105] S. Shen, A. Narayanaswamy, and G. Chen, Nano Lett. **9**, 2909–2913 (2009).
[106] A. W. Rodriguez, O. Ilic, P. Bermel, I. Celanovic, J. D. Joannopoulos, M. Soljačić, and S. G. Johnson, Phys. Rev. Lett. **107**, 114302 (2011).
[107] J.-M. Lourtioz, Photonic Crystals: Towards Nanoscale Photonic Devices (Springer Science and Business Media, Berlin, 2005).
[108] M. Florescu, H. Lee, A. Stimpson, and J. Dowling, Phys. Rev. A **72**, 33821 (2005).
[109] S. Han, Phys. Rev. B **80**, 1–10 (2009).
[110] M. G. Moharam and T. K. Gaylord, J. Opt. Soc. Am. **71**, 811 (1981).
[111] N. Nguyen-Huu, Y.-B. Chen, and Y.-L. Lo, Opt. Express **20**, 5882–5890 (2012).
[112] M. Ghebrebrhan, P. Bermel, Y. X. Yeng, I. Celanovic, M. Soljačić, and J. D. Joannopoulos, Phys. Rev. A **83**, 33810 (2011).
[113] P. P. Banerjee and J. M. Jarem, Computational Methods for Electromagnetic and Optical Systems (CRC Press, Boca Raton, 2000).
[114] C. J. Schuler, C. Wolff, K. Busch, and M. Florescu, Appl. Phys. Lett. **95**, 241103 (2009).
[115] M. Florescu and K. Busch, J. Opt. A **11**, 114005 (2009).
[116] I. El-Kady, G. B. Farfan, R. Rammohan, and M. M. R. Taha, Appl. Phys. Lett. **93**, 153501 (2008).
[117] R. Marklein, in: Review of Radio Science: 1999–2002 URSI, edited by W. R. Stone (John Wiley and Sons, New York, 2002), pp. 201–244.
[118] D. Chan, M. Soljacić, and J. D. Joannopoulos, Opt. Express **14**, 8785–8796 (2006).
[119] J. B. Schneider, Understanding the Finite-Difference Time-Domain Method (Washington State University, Pullman, 2010). http://www.eecs.wsu.edu/~schneidj/ufdtd/
[120] C. Luo, A. Narayanaswamy, G. Chen, and J. D. Joannopoulos, Phys. Rev. Lett. **93**, 19–22 (2004).
[121] A. F. Oskooi, J. Roundy, M. Ibanescu, P. Bermel, J. D. Joannopoulos, and S. G. Johnson, Comput. Phys. Commun. **181**, 687–702 (2010).
[122] I. El-Kady, W. W. Chow, and J. G. Fleming, Phys. Rev. B **72**, 195110 (2005).
[123] C. H. Seager, M. B. Sinclair, and J. G. Fleming, Appl. Phys. Lett. **86**, 1–3 (2005).
[124] M.-L. Hsieh, J. Bur, Y.-S. Kim, and S.-Y. Lin, Opt. Lett. **38**, 911–913 (2013).
[125] I. Celanovic, F. O'Sullivan, N. Jovanovic, M. Qi, and J. G. Kassakian, Photonic Cryst. Mater. Nanostruct. **5450**, 416–422 (2004).
[126] V. Rinnerbauer, Y. X. Yeng, W. R. Chan, J. J. Senkevich, J. D. Joannopoulos, M. Soljačić, and I. Celanovic, Opt. Express **21**, 11482–11491 (2013).
[127] M. Florescu, H. Lee, I. Puscasu, M. Pralle, L. Florescu, D. Z. Ting, and J. P. Dowling, Sol. Energy Mater. Sol. Cells **91**, 1599–1610 (2007).
[128] M. Garín, D. Hernández, T. Trifonov, and R. Alcubilla, Sol. Energy Mater. Sol. Cells **134**, 22–28 (2015).
[129] S. E. Han, A. Stein, and D. J. Norris, Phys. Rev. Lett. **99**, 3–6 (2007).
[130] B. J. Wiley, D. Qin, and Y. Xia, ACS Nano **4**, 3554–3559 (2010).
[131] T. N. Oder, J. Shakya, J. Y. Lin, and H. X. Jiang, Appl. Phys. Lett. **83**, 1231 (2003).
[132] A. T. Heiniger, B. L. Miller, and P. M. Fauchet, Opt. Express **23**, 25072–25083 (2015).
[133] R. Shenoi, J. Rosenberg, T. Vandervelde, O. Painter, and S. Krishna, IEEE J. Quantum Electron. **46**, 1051–1057 (2010).
[134] J. Rosenberg, R. R. V. Shenoi, T. T. E. Vandervelde, S. Krishna, and O. Painter, Appl. Phys. Lett. **95**, 161101 (2009).
[135] Y. X. Yeng, M. Ghebrebrhan, P. Bermel, W. R. Chan, J. D. Joannopoulos, M. Soljačić, and I. Celanovic, Proc. Natl. Acad. Sci. USA **109**, 2280–2285 (2012).
[136] V. Rinnerbauer, Y. X. Yeng, J. J. Senkevich, J. D. Joannopoulos, M. Soljačić, and I. Celanovic, Proc. SPIE **8632**, 1–8 (2013).
[137] V. Stelmakh, V. Rinnerbauer, R. D. Geil, P. R. Aimone, J. J. Senkevich, J. D. Joannopoulos, M. Soljacic, and I. Celanovic, Appl. Phys. Lett. **103**, 0–4 (2013).
[138] C. J. Crowley, N. A. Elkouh, S. Murray, and D. L. Chubb, AIP Conf. Proc. **746**, 601–614 (2005).
[139] Z. Wang, T. S. Luk, Y. Tan, D. Ji, M. Zhou, Q. Gan, and Z. Yu, Appl. Phys. Lett. **106**, 101104 (2015).

[140] J. A. Mason, D. C. Adams, Z. Johnson, S. Smith, A. W. Davis, and D. Wasserman, Opt. Express **18**, 25192–25198 (2010).
[141] P. Nagpal, S. E. Han, A. Stein, and D. J. Norris, Nano Lett. **8**, 3238–3243 (2008).
[142] K. A. Arpin, M. D. Losego, and P. V. Braun, Chem. Mater. **23**, 4783–4788 (2011).
[143] B. J. Lee and Z. M. Zhang, J. Appl. Phys. **100**, 1–10 (2006).
[144] F. O'Sullivan, I. Celanovic, N. Jovanovic, J. Kassakian, S. Akiyama, and K. Wada, J. Appl. Phys. **97**, 33529 (2005).
[145] S. G. Babiker, Y. Shuai, M. O. Sid-Ahmed, and M. Xie, in: 16th Int. Multi Top. Conf. (2014), pp. 97–103, DOI:10.1109/INMIC.2013.6731346.
[146] O. Ilic, P. Bermel, G. Chen, J. D. Joannopoulos, I. Celanovic, and M. Soljačić, Nature Nanotechnol. **11**, 320–324 (2016).
[147] W. R. Chan, P. Bermel, R. C. N. Pilawa-Podgurski, C. H. Marton, K. F. Jensen, J. J. Senkevich, J. D. Joannopoulos, M. Soljacic, and I. Celanovic, Proc. Natl. Acad. Sci. **110**, 5309–5314 (2013).
[148] B. J. Lee and Z. M. J. Zhang, Heat Transfer **129**, 17 (2007).
[149] A. Battula and S. C. Chen, Phys. Rev. B. **74**, 245407 (2006).
[150] A. Narayanaswamy and G. Chen, Phys. Rev. **70**, 1–4 (2004).
[151] E. R. Brown and O. B. McMahon, Appl. Phys. Lett. **67**, 2138 (1995).
[152] I. El-Kady, M. M. Sigalas, R. Biswas, K. M. Ho, and C. M. Soukoulis, Phys. Rev. B **62**, 15299–15302 (2000).
[153] M. Fujita, Y. Tanaka, and S. Noda, IEEE J. Sel. Top. Quantum Electron. **14**, 1090–1097 (2008).
[154] M. Araghchini, Y. X. Yeng, N. Jovanovic, P. Bermel, L. A. Kolodziejski, M. Soljacic, I. Celanovic, and J. D. Joannopoulos, J. Vac. Sci. Technol. B **29**, 61402 (2011).
[155] H. Qiao, J. Yang, F. Wang, Y. Yang, and J. Sun, Opt. Express **23**, 26617 (2015).
[156] I. Celanovic, N. Jovanovic, and J. Kassakian, Appl. Phys. Lett. **92**, 193101 (2008).
[157] V. Rinnerbauer, S. Ndao, Y. X. Yeng, J. J. Senkevich, K. F. Jensen, J. D. Joannopoulos, M. Soljačić, I. Celanovic, and R. D. Geil, J. Vac. Sci. Technol. B **31**, 11802 (2013).
[158] Y. Nam, Y. X. Yeng, A. Lenert, P. Bermel, I. Celanovic, M. >Soljačić, and E. N. Wang, Sol. Energy Mater. Sol. Cells **122**, 287–296 (2014).
[159] Y. X. Yeng, W. R. Chan, V. Rinnerbauer, V. Stelmakh, J. J. Senkevich, J. D. Joannopoulos, M. Soljacic, and I. Čelanović, Opt. Express **23**, A157 (2015).
[160] E. Homeyer, J. Houel, X. Checoury, G. Fishman, S. Sauvage, P. Boucaud, S. Guilet, R. Braive, A. Miard, A. Lemaître, and I. Sagnes, Phys. Rev. B **78**, 165305 (2008).
[161] H. Ye, H. Wang, and Q. J. Cai, Quantum Spectrosc. Radiat. Transf. **158**, 119–126 (2015).
[162] V. Stelmakh, W. R. Chan, M. Ghebrebrhan, M. Soljacic, J. D. Joannopoulos, and I. Celanovic, J. Phys. Conf. Ser. **660**, 012080 (2015).
[163] V. Stelmakh, V. Rinnerbauer, W. R. Chan, J. J. Senkevich, J. D. Joannopoulos, M. Soljacic, and I. Celanovic, in: Proc. SPIE 9115, Energy Harvesting and Storage: Materials, Devices, and Applications V (2014), p. 911504.
[164] R. Biswas, C. G. Ding, I. Puscasu, M. Pralle, M. McNeal, J. Daly, A. Greenwald, and E. Johnson, Phys. Rev. **74**, 1–6 (2006).
[165] M. C. F. Dobbelaar, S. Greveling, and D. van Oosten, Opt. Express **23**, 7481–7499 (2015).
[166] S. Prorok, Photonic Crystal Cavities – Nanophotonics and Integrated Optics (CST AG, Darmstadt, 2013), www.cst.com
[167] J. Song, H. Wu, Q. Cheng, and J. Zhao, J. Quantum Spectrosc. Radiat. Transf. **158**, 136–144 (2015).
[168] B. Zhao, L. Wang, Y. Shuai, and Z. M. Zhang, Int. J. Heat Mass Transf. **67**, 637–645 (2013).
[169] B. Zhao and Z. M. J. Zhang, J. Quantum Spectrosc. Radiat. Transf. **135**, 81–89 (2014).
[170] F. Han, X. Sun, L. Wu, and Q. Li, Opt. Express **21**, 28570 (2013).
[171] J. Wu, Opt. Commun. **355**, 246–250 (2015).
[172] W. Streyer, S. Law, A. Rosenberg, C. Roberts, V. A. Podolskiy, A. J. Hoffman, and D. Wasserman, Appl. Phys. Lett. **104**, 131105 (2014).
[173] J. Liu, U. Guler, A. Lagutchev, A. V. Kildishev, O. Malis, A. Boltasseva, and V. M. Shalaev, Opt. Mater. Express **5**, 1548–1551 (2015).
[174] M. D. Seal, N. R. Murphy, J. P. Lombardi, and M. A. Marciniak, Infrared Phys. Technol. **67**, 250–255 (2014).
[175] T. Inoue, T. Asano, M. De Zoysa, A. Oskooi, and S. J. Noda, Opt. Soc. Am. B **30**, 165 (2012).
[176] H. Wang, Y. Yang, and L. Wang, J. Opt. **17**, 1–6 (2015).
[177] Y. B. Chen and Z. M. Zhang, J. Phys. D: Appl. Phys. **41**, 95406 (2008).
[178] Y. Yang, F. Hou, S. Wu, W. Huang, M. Lai, and Y. Huang, Appl. Phys. Lett. **94**, 41122–41123 (2009).
[179] S. Takahashi, K. Suzuki, M. Okano, M. Imada, T. Nakamori, Y. Ota, K. Ishizaki, and S. Noda, Nature Mater. **8**, 721–725 (2009).
[180] G. B. Farfan, M. F. Su, M. M. Reda Taha, and I. El-Kady, Proc. SPIE 7609, Photonic and Phononic Crystal Materials and Devices X, 76090V (2010).
[181] P. Nagpal, D. P. Josephson, N. R. Denny, J. DeWilde, D. J. Norris, and A. Stein, J. Mater. Chem. **21**, 10836 (2011).
[182] N. R. Denny, F. Li, D. J. Norris, and A. Stein, J. Mater. Chem. **20**, 1538–1545 (2010).
[183] D. R. Smith, W. J. W. Padilla, D. C. Vier, S. C. Nemat-Nasser, and S. Schultz, Phys. Rev. Lett. **84**, 4184–4187 (2000).
[184] J. Pendry and D. R Smith, Phys. Today **57**, 36–43 (2004).
[185] N. Landy and D. R. Smith, Nature Mater. **12**, 25–28 (2013).
[186] N. Fang and X. Zhang, Appl. Phys. Lett. **82**, 161 (2003).
[187] S. Song, Q. Chen, L. Jin, and F. Sun, Nanoscale **5**, 9615–9619 (2013).
[188] W. Li and J. Valentine, Nano Lett. **14**, 3510–3514 (2014).
[189] M. K. Hedayati, A. U. Zillohu, T. Strunskus, F. Faupel, and M. Elbahri, Appl. Phys. Lett. **104**, 41103 (2014).
[190] E. Almpanis and N. Papanikolaou, J. Appl. Phys. **114**, 83106 (2013).
[191] C. Shemelya, D. F. DeMeo, and T. E. Vandervelde, Appl. Phys. Lett. **104**, 201113 (2014).
[192] P. Gay-Balmaz and O. J. F. Martin, J. Appl. Phys. **92**, 2929 (2002).
[193] N. I. Landy, S. Sajuyigbe, J. J. Mock, D. R. Smith, and W. Padilla, J. Phys. Rev. Lett. **100**, 207402 (2008).
[194] Q. Shen, B. Hou, Z. Chen, and Z.-L. Wang, AIP Adv. **2**, 42175 (2012).
[195] H. Merbold, A. Bitzer, F. Carbone, A. Murk, J. Wallauer, M. Walther, and T. Feurer, in: Proc. SPIE 8260, Ultrafast

Phenomena and Nanophotonics XVI, 826016 (2012). DOI:10.1117/12.908107.
[196] C. M. Watts, X. Liu, and W. Padilla, J. Adv. Mater. **24**, OP98-120, OP181 (2012).
[197] D. R. Smith and S. Schultz, Phys. Rev. B **65**, 195104 (2002).
[198] A. Sakurai, B. Zhao, and Z. M. Zhang, in: Proc. The 15th International Heat Transfer Conference (Kyoto, Japan, 2014), IHTC15-9012.
[199] A. Sakurai, B. Zhao, and Z. M. Zhang, J. Quantum Spectrosc. Radiat. Transf. **149**, 33–40 (2014).
[200] A. Sakurai, B. Zhao, and Z. M. Zhang, J. Quantum Spectrosc. Radiat. Transf. **158**, 111–118 (2015).
[201] N. A. Pfiester, Optimization of Metamaterial Selective Emitters for Use in Thermophotovoltaic Applications (Tufts University, Medford, 2016).
[202] X. Liu, T. Tyler, T. Starr, A. Starr, N. Jokerst, and W. Padilla, Phys. Rev. Lett. **107**, 4–7 (2011).
[203] C. Wu, B. Neuner III, J. John, A. Milder, B. Zollars, S. Savoy, and G. Shvets, J. Opt. **14**, 24005 (2012).
[204] J.-Y. Chang, Y. Yang, and L. Wang, Int. J. Heat Mass Transf. **87**, 237–247 (2015).
[205] L. Mo, L. Yang, E. H. Lee, and S. He, Plasmonics **10**, 529–538 (2015).
[206] D. Woolf, J. Hensley, J. G. Cederberg, D. T. Bethke, A. D. Grine, and E. A. Shaner, Appl. Phys. Lett. **105**, 81110 (2014).
[207] J. A. Mason, S. Smith, and D. Wasserman, Appl. Phys. Lett. **98**, 241105 (2011).
[208] W. Streyer, K. Feng, Y. Zhong, A. J. Hoffman, and D. Wasserman, Appl. Phys. Lett. **107**, 81105 (2015).
[209] B. Wang, X. Zhai, G. Wang, W. Huang, and L. Wang, Opt. Mat. Express **5**, 11147–11152 (2015).
[210] T. Cao, L. Zhang, R. E. Simpson, and M. J. Cryan, J. Opt. Soc. Am. **B30**, 1580–1585 (2013).
[211] A. I. Medina Ayala, Metamaterial Absorber Design and Implementation for Cruise Control Radar Applications (Tufts University, Medford, 2009).
[212] H. H. Tao, C. M. Bingham, A. C. Strikwerda, D. Pilon, D. Shrekenhamer, N. I. Landy, K. Fan, X. Zhang, W. J. Padilla, and R. D. Averitt, Phys. Rev. B **78**, 241103 (2008).
[213] J. Hao, J. Wang, X. Liu, W. J. Padilla, L. Zhou, and M. Qiu, Appl. Phys. Lett. **96**, 251104 (2010).
[214] H. Tao, N. I. Landy, C. M. Bingham, X. Zhang, R. D. Averitt, and W. J. Padilla, Opt. Express **16**, 7181 (2008).
[215] S. Linden, C. Enkrich, M. Wegener, J. Zhou, T. Koschny, and C. M. Soukoulis, Science **306**, 1351–1353 (2004).
[216] C. M. Shemelya, Photonics: Photodiodes and Metamaterials for Thermophotovoltaics and Photodetection Applications (Tufts University, Medford, 2013).
[217] C. Lin, R. Chern, and H. Lin, Opt. Soc. **19**, 686–688 (2011).
[218] H. Luo, Y. Z. Cheng, and R. Z. Gong, Eur. Phys. J. B **81**, 387–392 (2011).
[219] Y.-J. Huang, G. J. Wen, J. Li, W. R. Zhu, P. Wang, and Y. H. Sun, J. Electromagn. Waves Appl. **27**, 552–559 (2013).
[220] M. J. Lockyear, A. P. Hibbins, J. R. Sambles, P. A. Hobson, and C. R. Lawrence, Appl. Phys. Lett. **94**, 41913 (2009).
[221] B. Zhu, Z. Wang, C. Huang, Y. Feng, J. Zhao, and T. Jiang, Prog. Electromagn. Res. **101**, 231–239 (2010).
[222] H. Zhai, Z. Li, L. Li, and C. Liang, Microw. Opt. Technol. Lett. **55**, 1606–1609 (2013).
[223] B.-X. Wang, L. Wang, G. Wang, W. Huang, X. Li, and X. Zhai, Eur. Phys. J. B **87**, 98 (2014).
[224] W. Zhu and X. Zhao, J. Opt. Soc. Am. B **26**, 2382 (2009).
[225] B. Zhang, J. Hendrickson, and J. Guo, J. Opt. Soc. Am. B **30**, 656 (2013).
[226] J. W. Park, P. V. Tuong, J. Y. Rhee, K. W. Kim, W. H. Jang, E. H. Choi, L. Y. Chen, and Y. Lee, Opt. Express **21**, 9691–9702 (2013).
[227] B. Ni, X. S. Chen, L. J. Huang, J. Y. Ding, G. H. Li, and W. Lu, Opt. Quantum Electron. **45**, 747–753 (2013).
[228] Z. H. Jiang, S. Yun, F. Toor, D. H. Werner, and T. S. Mayer, ACS Nano **5**, 4641–4647 (2011).
[229] H. Cheng, S. Chen, H. Yang, J. Li, X. An, C. Gu, and J. Tian, J. Opt. **14**, 85102 (2012).
[230] H. Tao, C. M. Bingham, D. Pilon, K. Fan, A. C. Strikwerda, D. Shrekenhamer, W. J. Padilla, X. Zhang, and R. D. Averitt, J. Phys. D: Appl. Phys. **43**, 225102 (2010).
[231] J. A. Bossard and D. H. Werner, Opt. Express **21**, 3872–3884 (2013).
[232] J. A. Bossard and D. H. Werner, Opt. Express **21**, 5215–5225 (2013).
[233] S. L. Wadsworth, P. G. Clem, E. D. Branson, and G. D. Boreman, Opt. Mater. Express **1**, 466 (2011).
[234] R. L. Haupt and D. H. Werner, Genetic Algorithms in Electromagnetics (Wiley, 2007).
[235] H. Deng, T. Wang, J. Gao, and X. Yang, J. Opt. **16**, 35102 (2014).
[236] B. Neuner, C. Wu, G. T. Eyck, M. Sinclair, I. Brener, and G. Shvets, Appl. Phys. Lett. **102**, 2011–2015 (2013).

